Hydrodynamic forces on randomly formed marine aggregates

Eunji Yoo, Shilpa Khatri, and François Blanchette

Hydrodynamic forces on randomly formed marine aggregates

Eunji Yoo, Shilpa Khatri, and François Blanchette

March 17, 2020

Abstract

We study numerically the fluid forces acting on aggregates formed by a collation of cubic particles as a model of marine aggregates in the ocean. The flow around the aggregates and the resulting stresses on the surface of the aggregates are computed in the limit of zero Reynolds number using a boundary integral method, resulting in an accurate evaluation of the flow around fractal objects. We compare a single- and double-layer integral method to compute the velocity and determine that the single-layer approach is more suitable to capturing the flow around aggregates. We then characterize the drag of translation flows, the torque of rotational flows, and the straining force of extensional flows acting on aggregates as a function of their size and mode of formation. We determine that the force and torque are best characterized using the gyration radius of the aggregates, and the straining force is better characterized by the maximal radius.

1   Introduction

Marine aggregates play a major role in the removal of carbon dioxide from the atmosphere [1]. In the surface ocean, dissolved carbon dioxide is in equilibrium with atmospheric carbon dioxide. Phytoplankton living in the surface ocean absorb the dissolved carbon dioxide. These phytoplankton play several roles within the marine ecosystem, including serving as food for zooplankton [2], breaking down under bacterial activity [3], and most significant for carbon removal, becoming a component of marine aggregates [4]. These marine aggregates eventually settle from the surface to the deep ocean, effectively removing the carbon dioxide from the atmospheric carbon cycle [5]. The focus of the present paper is to study, using computational simulations, the dynamics of marine aggregates in flow.

Marine aggregates form through the random accumulation of various particulates floating in seawater and are mostly composed of phytoplankton, detritus, sediment, and fecal pellets [6]. These components stick together due to extracellular polymeric substances, mucus-like substances, produced by phytoplankton and bacteria. The resulting aggregates are found to range in size from approximately 100 microns to a couple of centimeters [4] and are usually more than 99% porous [4], resulting in very slow settling speeds. Moreover, it is well established that marine aggregates found in the ocean often have a fractal structure [4, 6].

In the last few decades, several scientists have modeled the dynamics and ecological impact of marine aggregates [6, 3]. Their effects on bacterial transport [7] and algal bloom [8] have been described in models that use simplified descriptions of the aggregates' settling speeds. Moreover, accumulation of aggregates in thin layers where the ambient fluid is stratified have been reported [9, 10] and more recently modeled experimentally [11], analytically [12], and computationally [13]. Understanding the formation and persistence

of these thin layers is ecologically important. However, simplifying assumptions have to be made to capture these intricate dynamics. Most importantly, the aggregates settling speed is often approximated based on their size. To be useful, these necessary simplifications require an accurate correspondence between an actual aggregate and an effective hydrodynamic radius. A well-chosen hydrodynamic radius preserves properties, such as the force and torque on the object. One of the objectives of this work is to provide more complete and accurate data allowing the determination of a hydrodynamic radius of an aggregate in a variety of contexts.

In this paper, we compute the flow around randomly-formed aggregates and characterize the resulting hydrodynamic forces. Since the 1980s, there have been numerous models of aggregation, including marine aggregation, based on the random motion of small particulates [14, 15, 16, 17]. To form aggregates, we use two established models: individually-added aggregation and cluster-cluster aggregation, which we describe in detail in Section 2. We study the hydrodynamics of flow around a broad sample of the resulting aggregates. In situ measurements of oceanic aggregates have shown an approximately linear relationship between the drag and the aggregate diameter [4]. Experimental studies of settling aggregates first focused on inorganic clusters [18] and later considered precisely constructed aggregates [19] and statistical descriptions of broader ensembles [20]. It was generally found that a linear relation exists between the drag and the square root of the projected area, which allows for the identification of a corresponding settling hydrodynamic radius [20, 21]. However, these experimental studies did not allow for a systematic variation of certain parameters and found a range of results, depending on the measure used and the exact composition of the aggregates. Computational studies, in theory, do not have this limitation. Early numerical results were based on rather coarse approximations of aggregates, using point particle approximations [22]. The accelerated Stokesian dynamics (ASD) approach, which model aggregates as a collection of spheres and accounts for lubrication forces between them, was later developed [23] and used to estimate a hydrodynamic radius for progressively larger aggregates [24, 25]. In addition to the drag on settling aggregates, the torque on rotating aggregates was computed using ASD [26]. More recently, results were obtained using Lattice-Boltzmann simulations that also considered inertial effects [27]. The distribution of internal stresses in rigid aggregates moving in a constant flow, which may result in aggregate break-up, was also recently studied using the method of reflections [28] and again using ASD [29]. We develop here computational simulations that, in the regime considered, are more flexible and efficient, allowing us to study a greater number of aggregates, resulting in more statistically reliable results.

We consider flow around aggregates in the low Reynolds number regime, which is applicable for approximately the smallest 30% of marine aggregates [4]. Flow in this regime is governed by the Stokes equations, which allows solutions to be found via boundary integral methods [30]. Such methods have been implemented in several different contexts, typically via a combination of analytical integration near the singularities that arise and quadrature methods away from the singularities, see [31] for a review. Boundary integral methods are particularly well suited to computations of flow around complex solids [32] as velocity and forces may be expressed in terms of an integral over the boundary of the object. They have also recently been combined with other methods, for example to capture interactions between fluids and elastic solids [33] and stochastic fluctuations in suspensions [34]. Here, we form aggregates using cubic particles, which results in a simple boundary over which the resulting integrals can be computed analytically, as described in Section 3. This has the advantage of avoiding numerical singularities on the boundary, which otherwise require regularization [35] or specialized numerical methods such as high-order product Nyström methods [36, 37], adaptive sub-domain integration [38], or nearest-neighbor discretization of the regularized Stokeslet boundary integral equation [39]. We introduce a novel implementation of boundary integral methods which is both simple and well-behaved numerically. Details of this new methodology, along with its validation are presented in Section 4. We compare two approaches, using a single-layer and double-layer integral representation of the velocity [30, 40, 41], and determine which is the most suitable for fluid flow simulations around marine aggregates with this new method.

Using our new numerical method, we characterize the forces acting on marine aggregates of various sizes

and of two different fractal dimensions in Section 5. We consider a linear approximation of a general flow and therefore consider aggregates that are settling, rotating, or subject to a straining flow. We compute the resulting hydrodynamic force, torque, and straining force acting on aggregates. The efficiency of the method allows us to consider a large number and broad range of aggregates. We determine the most suitable measure of an aggregate's size in various contexts, comparing the projected area, maximum radius, and gyration radius. In Section 6, we discuss the scaling of our results and compare them to corresponding results for spheres, allowing the determination of an effective hydrodynamic radius. We present our conclusions in Section 7.
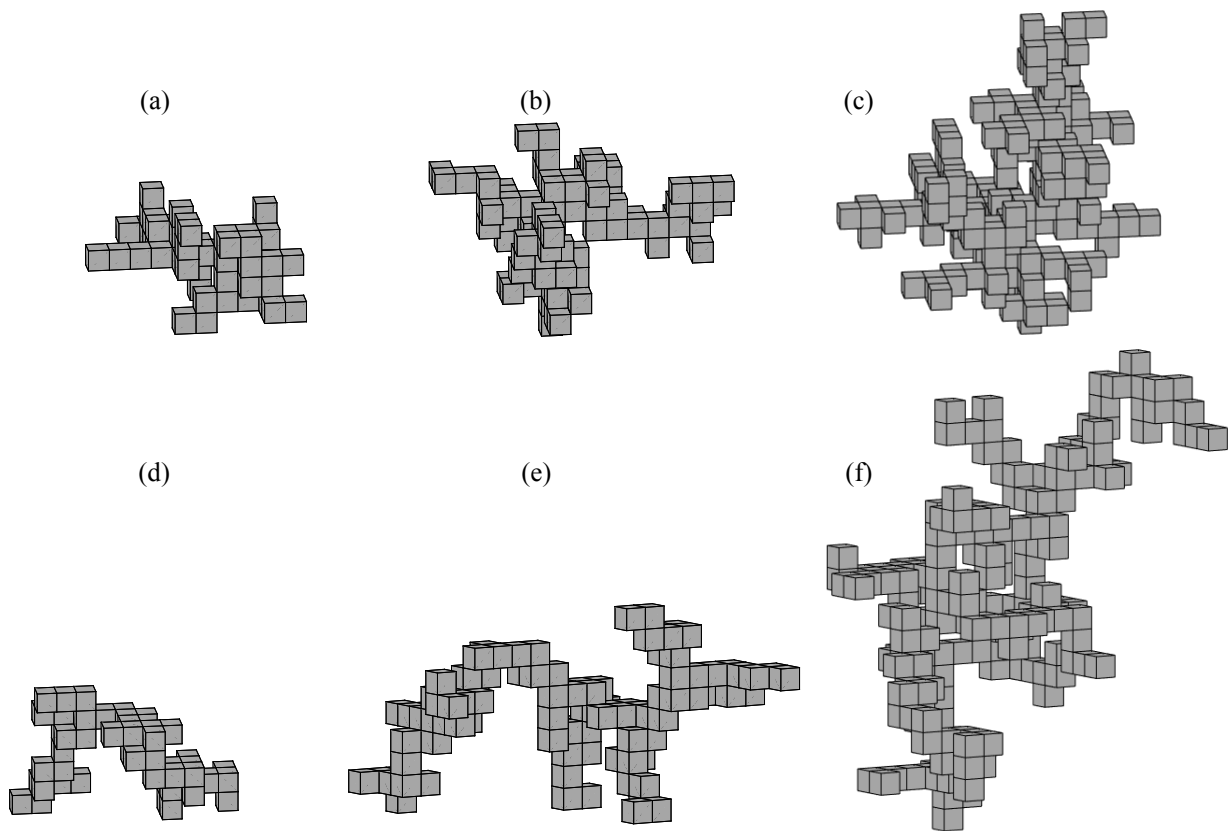
2 Aggregation Model

Figure 1: We show typical aggregates as formed by two different methods. Top row: individually-added-aggregates (IAA) containing (a) 50, (b) 100, and (c) 200 cubes. Bottom row: cluster-to-cluster aggregates (CCA) containing (d) 50, (e) 100, and (f) 200 cubes.

To model marine aggregates, we make use of existing models of aggregation where the constituting particles undergo a random walk [14, 15, 16, 17]. In these models, particles are typically subject to uniform Brownian motion and attach to one another when sufficiently close. The resulting aggregates often have a fractal structure, characterized by a fractal dimension, d. The fractal dimension describes the nature of these complicated objects and may be defined from the relation $N \sim (R_s/l)^d$, where N is the number of

particles of length scale l that are part of the aggregate within a sphere of radius R_s [16]. In general, fractal dimensions of aggregate models have been found to range from 1.3 to 3 depending on the exact formation mechanism [15, 17, 42]. Direct observations of marine aggregates have found fractal dimensions ranging approximately from 1.3 to 2.5 [4, 6].

We consider aggregates made of collated cubic particles, as shown in Fig. 1. Once formed, we assume that aggregates do not deform, sinter, or break apart [43]. This is a flexible model that has the advantage of having a simple external boundary, which will be exploited when we solve for the flow around the aggregate. We generate diffusion-limited aggregates using two different techniques: (1) individually-added aggregation and (2) cluster-to-cluster aggregation [16, 17]. In both methods, each cube has non-dimensional length, 2, is aligned with the Cartesian axes, and is centered at a point on a three-dimensional Cartesian lattice restricted to a triply periodic box of period $2P$. The cube centers thus only take values of the form $\{(2m, 2n, 2p) \,|\, m, n, p \in \mathbb{Z}, -P < m, n, p \leq P\}$.

For individually-added aggregates (IAA), we initiate aggregate formation by placing one cube at the center of the periodic box. A second cube is then introduced at a random location within the periodic box, with the exclusion of the aggregate and its immediately adjacent cells. This newly introduced cube then undergoes a random walk on the periodic Cartesian lattice. The random walk is unbiased, with a 1/6 probability of moving by two units in any direction on the lattice. When the random walker arrives at a location neighboring the existing aggregate, it attaches to the aggregate and stops moving. A new cube is then randomly introduced and the process is repeated. Examples of aggregates formed using this methodology with 50, 100, and 200 cubes are shown in Fig. 1(a)-1(c). Aggregates formed in this manner have a fractal structure with a fractal dimension that has been measured to be 2.5 and 3 [44]. Below, we give our own estimation of the fractal dimension.
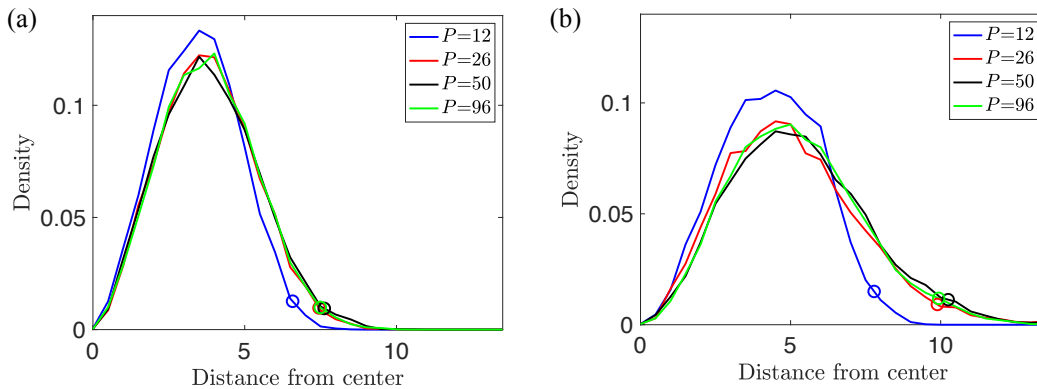

Figure 2: Distribution of the non-dimensional distance between each constituting cube and the aggregate's center of mass. Here each aggregate is made of $N = 100$ cubes and the periodic domain size, P, is varied. The density was calculated using 400 aggregates of each type. We show in (a) individually-added-aggregates (IAA) and in (b) cluster-to-cluster aggregates (CCA). The circles indicate the maximum distance to the center of mass within a given aggregate, averaged over 400 aggregates.

As a second aggregation mechanism, we use cluster-to-cluster aggregation (CCA). In this case, we initially position N cubes at random, non-adjacent, locations within the periodic domain. Each of the N cubes then undergoes, in turn, an unbiased random walk on the periodic lattice as was the case for individual cubes in IAA. If at any time any two cubes neighbor each other, they form a cluster. Clusters continue to undergo the same random walk, with the entire cluster moving in the same direction, and each cluster moving in turn. The process stops when a single aggregate encompassing the N initial cubes is obtained. Examples of aggregates formed using this methodology with $N = 50, 100$, and 200 are shown in Fig. 1(d)-1(f). This type
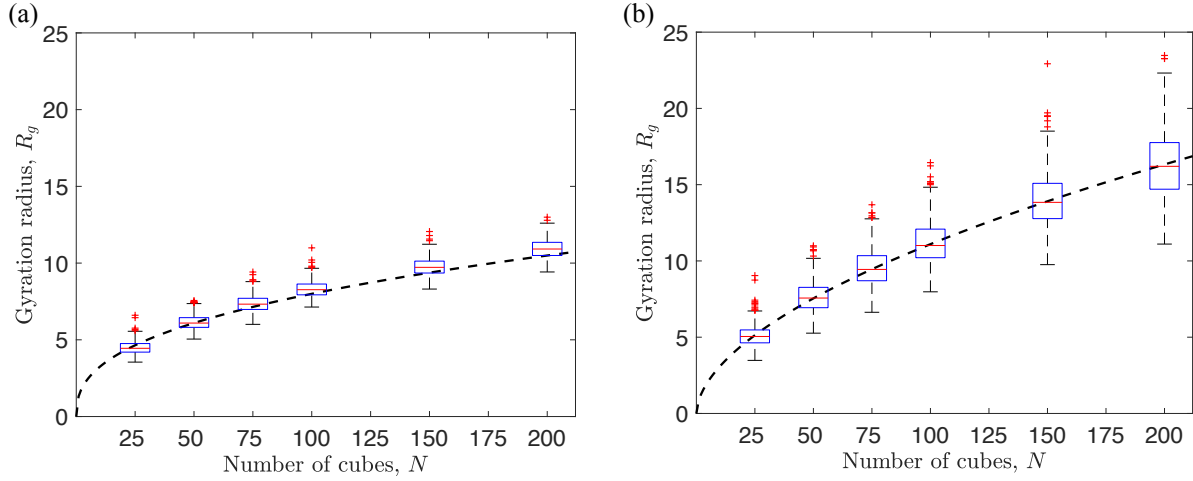
4

Figure 3: Non-dimensional gyration radius of aggregates, R'_g, as a function of the number of cubes within the aggregates. We present in (a) individually-added-aggregates (IAA) and in (b) cluster-cluster aggregates (CCA). Each box has height given by one standard deviation and is centered around the mean as observed in 400 sample aggregates. The dashed lines are the loglog fits of the mean gyration radius as a function of N.

of aggregate has been found to have fractal dimension between 1.6 and 2.2 [15].

To characterize the size of each aggregate, we define the dimensionless gyration radius, R'_g, also known as the root-mean-square radius as,

$$R'_g = \sqrt{\frac{1}{N} \sum_{k=1...N} ||\vec{x}_k - \vec{x}_{cm}||^2}, \tag{1}$$

where the sum is taken over all N cubes forming an aggregate, each with center position $\vec{x}_k$, and where $\vec{x}_{cm} = \frac{1}{N} \sum_{k=1}^{N} \vec{x}_k$ is the position of the center of mass of the entire aggregate. Here, quantities have been made dimensionless using the half-width of the cubic particles, L, forming the aggregates, so that the edge of each cube has length $2L$ and dimensionless length 2. The prime notation indicates a dimensionless quantity. We also measure the size of each aggregate using a dimensionless maximum radius, R'_m. The maximum radius of the aggregate is defined as the maximum of the distances between the center of each of its constituting cubes and the center of mass, to which we add one to account for the size of an individual cube,

$$R'_m = 1 + \max_{k=1...N} ||\vec{x}_k - \vec{x}_{cm}||. \tag{2}$$

Both measures of size are used to characterize an aggregate, and we will later discuss which measure best captures the response of an aggregate to different background flows. Note that it is also possible to describe aggregates using their projected area A'_p, which is the area of the projection of the aggregate on a predetermined plane.

We plot the distribution of the distance $||\vec{x}_k - \vec{x}_{cm}||$ for various periods P in Fig. 2. When the period is small, $P = 12$, the random initial location of the cubes can affect the shape of the resulting aggregates. However, for larger periods, we see that the statistics of the aggregates do not depend on the exact choice of the period. In the remainder of this paper, we have used $P = 50$.

In Fig. 3, we present the distribution of the gyration radius as a function of the number of cubes in an aggregate for IAA and CCA. Fitting a loglog curve through this data, we find that the gyration radius is

approximately, $R'_g = 1.32N^{0.39}$ for IAA, corresponding to a fractal dimension of $d_{IAA} = 1/0.39 = 2.56$. For CCA, the gyration radius is approximately, $R'_g = 0.85N^{0.56}$, corresponding to a fractal dimension of $d = 1/0.56 = 1.79$. These fits are shown as the dashed curves in Fig. 3(a) and 3(b), respectively. Note that the IAA are significantly more compact than the CCA. The CCA also show a much broader size distribution for a given number of cubes. We note that using the maximum radius as a measure of length instead of the gyration radius yielded similar fractal dimensions of 2.45 and 1.77, for IAA and CCA, respectively. These results are in good agreement with previously obtained fractal dimensions given above [15, 45].

3   Fluid Equations and Hydrodynamic Forces

Marine aggregates are nearly impermeable, but very porous, with porosity on the order of 99% of the aggregate [4]. They are therefore nearly filled with water, and are only barely denser than the surrounding fluid, with a typical measured density difference on the order of 0.1kg/m^3. In this paper we consider relatively small marine aggregates, with a maximal radius of about $R = 500\mu$m (or a diameter of 1mm), which describe approximately the smallest 30% of aggregates found at a depth of about 10m [4]. For aggregates of such sizes or smaller and using typical seawater density, $\rho = 1020$ kg/m^3, and viscosity, $\mu = 1.2 \times 10^{-3}$kg/ms, we find an approximate Reynolds number of $Re = \frac{\rho U_s R}{\mu} \leq 0.05$, where U_s is the aggregate settling speed. Since $Re \ll 1$, we may neglect inertial effects and model the fluid flow around these aggregates using the Stokes equations,

$$\nabla \cdot \vec{u} = 0 \tag{3}$$
$$-\nabla P_d + \mu \nabla^2 \vec{u} = 0 \tag{4}$$

where $\vec{u}$ is the velocity of the fluid and P_d is the dynamic pressure. In the presence of gravity, acting in direction $\vec{g}$, the dynamic pressure is defined at a point $\vec{x}_0$ in the fluid as $P_d(\vec{x}_0) = P(\vec{x}_0) + \rho\vec{g} \cdot \vec{x}_0$, where P is the fluid pressure. The density, ρ, and viscosity, μ, are assumed to be constant.
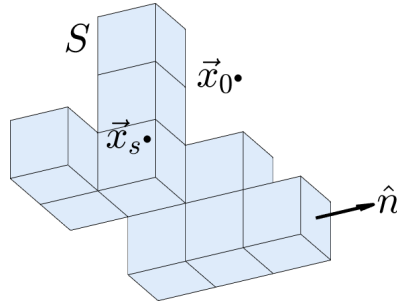

Figure 4: Schematic of the domain under consideration. We solve for the fluid velocity at points $\vec{x}_s$ that lie on the surface, S, and at points, $\vec{x}_0$, that are exterior to S. The outward normal to the surface is denoted by $\hat{n}$.

We are interested in solving for the flow at points $\vec{x}_0$ in the fluid domain extending to infinity and external to the surface, S, of an aggregate, as shown in Fig. 4. We take advantage of the linearity of the Stokes equations and express the velocity as a boundary integral over the surface of the aggregate [30, 46]. The resulting Fredholm integral formulae have the advantage of involving computations in two dimensions only,

despite the three-dimensionality of the system. For solid objects, one may obtain two different Fredholm integral formulae. We introduce both formulations in the remainder of this section, and compare them in the following section.

For a general surface S, the velocity at a point $\vec{x}_0$ exterior to the surface may generally be expressed using the representation formula [30],

$$\vec{u}(\vec{x}_0) = -\int_S \vec{f}(\vec{x}) \cdot \bar{\bar{G}}(\vec{x}, \vec{x}_0) \, \mathrm{d}S(\vec{x}) + \int_S \vec{u}(\vec{x}) \cdot \bar{\bar{K}}(\vec{x}, \vec{x}_0) \cdot \hat{n} \, \mathrm{d}S(\vec{x}), \tag{5}$$

where the integral is taken over points $\vec{x}$ on the surface S. The kernel $\bar{\bar{G}}(\vec{x}, \vec{x}_0)$ is the Green's function of the Stokes equations (a single-layer potential) at any point $\vec{x}_0$ in the domain for a point-source located at $\vec{x}$. The kernel $\bar{\bar{K}}(\vec{x}, \vec{x}_0)$ is the stress tensor associated to this fundamental solution (a double-layer potential). We give explicit expressions for $\bar{\bar{G}}(\vec{x}, \vec{x}_0)$ and $\bar{\bar{K}}(\vec{x}, \vec{x}_0)$ below. Also, $\vec{f}(\vec{x})$ is the generally unknown stress vector, or traction, on the surface, and $\vec{u}(\vec{x})$ is the, generally unknown, velocity on the surface S. When S is the boundary of a solid object, in our case an aggregate, the general representation formula may be simplified in two different ways.

3.1 Single-layer potential

The first simplification we consider results in a boundary integral formulation involving a single-layer potential only. For a surface S corresponding to the boundary of a solid object, the double-layer integral in equation (5) is identically zero [30]. One can thus express the velocity at any point $\vec{x}_0$ that is either on or exterior to the boundary as

$$\vec{u}(\vec{x}_0) = -\int_S \vec{f}(\vec{x}) \cdot \bar{\bar{G}}(\vec{x}, \vec{x}_0) \, \mathrm{d}S(\vec{x}) = -\frac{1}{8\pi\mu} \int_S \vec{f}(\vec{x}) \cdot \left(\frac{\bar{\bar{I}}}{||\vec{x} - \vec{x}_0||} + \frac{(\vec{x} - \vec{x}_0)(\vec{x} - \vec{x}_0)}{||\vec{x} - \vec{x}_0||^3} \right) \, \mathrm{d}S(\vec{x}) \tag{6}$$

where we have substituted the definition of $\bar{\bar{G}}(\vec{x}, \vec{x}_0)$,

$$\bar{\bar{G}}(\vec{x}, \vec{x}_0) = \frac{1}{8\pi\mu} \left(\frac{\bar{\bar{I}}}{||\vec{x} - \vec{x}_0||} + \frac{(\vec{x} - \vec{x}_0)(\vec{x} - \vec{x}_0)}{||\vec{x} - \vec{x}_0||^3} \right). \tag{7}$$

To determine the unknown stress vector, $\vec{f}(\vec{x})$, we take advantage of the constraints on the velocity at the surface of a solid object. The velocity at any point $\vec{x}_s$ on the surface of a solid object can be expressed as

$$\vec{u}(\vec{x}_s) = \vec{U}_a + \vec{\Omega} \times (\vec{x}_s - \vec{x}_{cm}) \tag{8}$$

where $\vec{x}_{cm}$ is the position of the center of mass of the aggregate, $\vec{U}_a$ is the translation velocity of the aggregate, and $\vec{\Omega}$ is its angular velocity. These vectors are the same for all points on a given aggregate.

In general, one can determine $\vec{U}_a$ and $\vec{\Omega}$ using the property that forces in the inertia-free regime are always at equilibrium and assuming that a known force and torque are imposed on the object. The total force, $\vec{F}$, and the total torque, $\vec{Q}$, are related to the stress vector through

$$\vec{F} = \int_s \vec{f}(\vec{x}) \, \mathrm{d}S(\vec{x}) \qquad \text{and} \qquad \vec{Q} = \int_s (\vec{x} - \vec{x}_{cm}) \times \vec{f}(\vec{x}) \, \mathrm{d}S(\vec{x}). \tag{9}$$

If gravity is the only external force acting on the aggregate, we have, accounting for the use of a dynamic pressure, $\vec{F} = (\rho_s - \rho)V\vec{g}$, where ρ_s is the density of the aggregate and V its volume. Moreover, the torque is

then zero, $\vec{Q} = 0$. Using equation (6) at points on the boundary with equations (8) and (9), it is then possible to determine the stress vector, $\vec{f}(\vec{x})$, and the translation and angular velocities, respectively, $\vec{U}_a$ and $\vec{\Omega}$.

Alternatively, and as will be more convenient in the present study, $\vec{U}_a$ and $\vec{\Omega}$ may first be prescribed and equations (6) and (8) may be used at points on the aggregate surface to solve for the stress vector $\vec{f}(\vec{x})$. Equations (9) may then be used to determine the corresponding force and torque acting on the aggregate.

3.2 Double-layer potential

The second approach we consider eliminates the single-layer potential term, leaving only a double-layer potential to integrate. The result is a Fredholm integral of the second kind in terms of a generally unknown density function, $\vec{\psi}(\vec{x})$, (not to be confused with the fluid density, ρ) which now takes the place of the velocity as part of the integrand. As stated above, such integrals are identically zero on a solid object. However, as presented in [40], these integrals may be used to compute the correction to the flow induced by a point-force of magnitude $\vec{F}$ and a point-torque of magnitude $\vec{Q}$, so that the resulting flow satisfies the no-slip boundary conditions on S. The point-force and point-torque induce the correct far-field velocity, while the corrections decay more rapidly. Following the approach described by Power & Miranda [40], one may thus obtain an expression for the velocity field at any point $\vec{x}_0$ exterior to S as

$$\vec{u}(\vec{x}_0) = \int_S \vec{\psi}(\vec{x}) \cdot \bar{\bar{K}}(\vec{x}, \vec{x}_0) \cdot \hat{n} \, \mathrm{d}S(\vec{x}) + \vec{F} \cdot \bar{\bar{G}}(\vec{x}_0, \vec{x}_{cm}) + \frac{1}{8\pi\mu} \frac{\vec{Q} \times (\vec{x}_0 - \vec{x}_{cm})}{\|\vec{x}_0 - \vec{x}_{cm}\|^3}, \tag{10}$$

where $\vec{x}_{cm}$ is the center of mass of the aggregate and $\bar{\bar{K}}(\vec{x}, \vec{x}_0)$ is defined as

$$\bar{\bar{K}}(\vec{x}, \vec{x}_0) = -\frac{3}{4\pi} \frac{(\vec{x} - \vec{x}_0)(\vec{x} - \vec{x}_0)(\vec{x} - \vec{x}_0)}{\|\vec{x} - \vec{x}_0\|^5}, \tag{11}$$

where $\hat{n}$ is the unit normal directed from the object into the fluid. Moreover, the total force, $\vec{F}$, and total torque, $\vec{Q}$, are related to the unknown density through

$$\vec{F} = \frac{\mu}{L} \int_S \vec{\psi}(\vec{x}) \, \mathrm{d}S(\vec{x}), \qquad \text{and} \qquad \vec{Q} = \frac{\mu}{L} \int_S \vec{\psi}(\vec{x}) \cdot (\bar{\bar{\epsilon}} \cdot \vec{x}) \, \mathrm{d}S(\vec{x}), \tag{12}$$

where $\bar{\bar{\epsilon}}$ is the third-order permutation tensor and L is a measure of the aggregate's size. Here again we define L as the half-width of the cubic particles composing the aggregates, so that the edge of each cube has length $2L$. We note that our chosen relationships between the vectors $\vec{F}$ and $\vec{Q}$ and the density function $\vec{\psi}(\vec{x})$ differ slightly from those defined by [40], as these relationships can be defined up to an arbitrary multiplicative constant. We therefore choose to incorporate the factor of μ/L, to give these vectors units of force and torque, respectively. As stated above, when gravity is the only external force acting on the aggregate, $\vec{F} = (\rho_s - \rho)V\vec{g}$ and $\vec{Q} = 0$.

For points $\vec{x}_s$ located on the surface S, equation (10) is not valid due to the discontinuity of the integral of $\bar{\bar{K}}$ as $\vec{x}_0$ approaches S. In the limit of a point approaching the boundary, a jump proportional to the value of the density function occurs, leading to a modified formula for points on the surface S,

$$\vec{u}(\vec{x}_s) = -\frac{1}{2}\vec{\psi}(\vec{x}_s) + \int_S \vec{\psi}(\vec{x}) \cdot \bar{\bar{K}}(\vec{x}, \vec{x}_s) \cdot \hat{n} \, \mathrm{d}S(\vec{x}) + \vec{F} \cdot \bar{\bar{G}}(\vec{x}_s, \vec{x}_{cm}) + \frac{1}{8\pi\mu} \frac{\vec{Q} \times (\vec{x}_s - \vec{x}_{cm})}{\|\vec{x}_s - \vec{x}_{cm}\|^3}. \tag{13}$$

Given the total force and torque, one can then use equation (13) coupled with equations (8) and (12), to solve for the unknown density function, $\vec{\psi}(\vec{x})$, as well as $\vec{U}_a$ and $\vec{\Omega}$.

8

Alternatively, similarly to the single-layer case, $\vec{U}_a$ and $\vec{\Omega}$ can be prescribed, and equations (8) and (13) can be used to solve for the density function. Once $\vec{\psi}(\vec{x}_s)$ is known, equation (12) may be used to compute the resulting force and torque, and equation (10) can be used to determine the velocity of the fluid at any point exterior to the surface of the aggregate.

3.3 Non-dimensionalization

To write the equations given above in non-dimensional form, we use the fluid density, ρ, as a density scale and the half-width of the unit cubes used to assemble aggregates, L, as a length scale. For the velocity scale, we use the dimensional scaling of the Stokes settling speed, $U_s = \frac{g(\rho_s - \rho)L^2}{\mu}$. We may then define non-dimensional quantities, denoted with a prime, as

$$\vec{u} = U_s \vec{u}' \qquad \vec{f} = \frac{\mu U_s}{L} \vec{f}' \qquad \vec{x} = L\vec{x}', \qquad \vec{\psi} = U_s \vec{\psi}', \qquad \vec{F} = U_s \mu L \vec{F}', \qquad \vec{Q} = U_s \mu L^2 \vec{Q}'. \quad (14)$$

Equation (8), used in both the single-layer and double-layer formulations, is thus non-dimensionalized as

$$\vec{u}'(\vec{x}'_s) = \frac{\vec{U}_a}{U_s} + \frac{\vec{\Omega}L}{U_s} \times (\vec{x}'_s - \vec{x}'_{cm}) = \vec{U}'_a + \vec{\Omega}' \times (\vec{x}'_s - \vec{x}'_{cm}) \quad (15)$$

For the single-layer approach, we obtain a non-dimensional form of equation (6),

$$\vec{u}'(\vec{x}'_0) = -\frac{1}{8\pi} \int_{S'} \vec{f}'(\vec{x}') \cdot \left(\frac{\bar{\bar{I}}}{||\vec{x}' - \vec{x}'_0||} + \frac{(\vec{x}' - \vec{x}'_0)(\vec{x}' - \vec{x}'_0)}{||\vec{x}' - \vec{x}'_0||^3} \right) dS'(\vec{x}'). \quad (16)$$

The equations for the non-dimensional force and angular velocity, given dimensionally in equation (9), become

$$\vec{F}' = \vec{F} \frac{1}{\mu U_s L} = \int_{S'} \vec{f}'(\vec{x}') \, dS'(\vec{x}') \quad (17)$$

$$\vec{Q}' = \vec{Q} \frac{1}{\mu U_s L^2} = \int_{S'} (\vec{x}' - \vec{x}'_{cm}) \times \vec{f}'(\vec{x}') \, dS'(\vec{x}'). \quad (18)$$

We non-dimensionalize the double-layer approach in a similar manner. Thus, equations (10) and (13) become, respectively,

$$\vec{u}'(\vec{x}'_0) = \int_{S'} \vec{\psi}'(\vec{x}') \cdot \bar{\bar{K}}(\vec{x}', \vec{x}'_0) \cdot \hat{n} \, dS(\vec{x}') + \vec{F}' \cdot \bar{\bar{G}}(\vec{x}'_0, \vec{x}'_{cm}) + \frac{1}{8\pi} \frac{\vec{Q}' \times (\vec{x}'_0 - \vec{x}'_{cm})}{||\vec{x}'_0 - \vec{x}'_{cm}||^3} \quad (19)$$

for points $\vec{x}'_0$ outside the object and

$$\vec{u}'(\vec{x}'_s) = -\frac{1}{2} \vec{\psi}'(\vec{x}'_s) + \int_{S'} \vec{\psi}'(\vec{x}') \cdot \bar{\bar{K}}(\vec{x}', \vec{x}'_s) \cdot \hat{n} \, dS(\vec{x}') + \vec{F}' \cdot \bar{\bar{G}}(\vec{x}'_s, \vec{x}_{cm}) + \frac{1}{8\pi} \frac{\vec{Q}' \times (\vec{x}'_s - \vec{x}'_{cm})}{||\vec{x}'_s - \vec{x}'_{cm}||^3} \quad (20)$$

for points $\vec{x}'_s$ on the object. The non-dimensional point-force and torque, given dimensionally in equation (12) become

$$\vec{F}' = \int_{S'} \vec{\psi}'(\vec{x}') \, dS(\vec{x}') \quad (21)$$

$$\vec{Q}' = \int_{S'} \vec{\psi}'(\vec{x}') \cdot (\bar{\bar{\epsilon}} \cdot \vec{x}') \, dS(\vec{x}'). \quad (22)$$

4 Numerical Methods

As discussed above, when solving for the velocity field exterior to a solid object or an aggregate, one may either prescribe the translation velocity, $\vec{U}'_a$, and angular velocity, $\vec{\Omega}'$, of the object or prescribe the total force and torque. We found the analysis easier to perform when setting $\vec{U}'_a$ and $\vec{\Omega}'$ to known values, providing us with the velocity on the surface of the object via equation (15). We thus know $\vec{u}'$ on the left-hand-side of equations (16) and (20). Provided we can evaluate the surface integrals, we may then solve for the unknown stress vector, $\vec{f}'$, or density, $\vec{\psi}'$, respectively. Once these are found, we can evaluate the velocity of the fluid at any point exterior to the aggregate using equations (16) or (19) and compute the force and torque via equations (17) and (18) or equations (21) and (22).

Because we consider aggregates that are composed of cubic particles, their surface is simply a collection of squares. In both the single and double-layer potential approach we impose a velocity at the center of each square on the surface, $\vec{x}_{sq,i}$, where $i = 1, 2, \cdots, N_f$, with N_f denoting the total number of square faces of an aggregate. We thus need to compute integrals of the form

$$\vec{I}(\vec{x}'_{sq,i}) = \int_{S'} \vec{q}'(\vec{x}') \cdot \bar{\bar{J}}(\vec{x}', \vec{x}'_{sq,i}) \, \mathrm{d}S'(\vec{x}'). \tag{23}$$

Here, $\vec{q}$ represents either $\vec{f}$ or $\vec{\psi}$, and $\bar{\bar{J}}$ stands for either $\bar{\bar{G}}$ or $\bar{\bar{\bar{K}}} \cdot \hat{n}$, depending on if the single or double-layer method is used, respectively. To allow an exact analytic computation of the integrals, we assume that on the kth square face the vector $\vec{q}'(\vec{x}') = \vec{q}'_k$ is constant, for $k = 1, 2, \ldots, N_f$. The surface integrals over the entire aggregate may then be discretized as

$$\vec{I}(\vec{x}'_{sq,i}) = \sum_{k=1}^{N_f} \vec{q}'_k \int_{S'_k} \bar{\bar{J}}(\vec{x}', \vec{x}'_{sq,i}) \, \mathrm{d}S'(\vec{x}') = \sum_{k=1}^{N_f} \vec{q}'_k \, \bar{\bar{\Pi}}'_{i,k}. \tag{24}$$

where the coefficients $\bar{\bar{\Pi}}'_{i,k}$ are constant. These constants may be computed analytically, and the corresponding formulae are given in Appendix A. This discretization is equivalent to using a two-dimensional mid-point rule to estimate the integrals. Equation (24) is linear in $\vec{q}'_k$, resulting in a dense linear system of $3N_f$ equations for each of the N_f three-dimensional unknown vectors $\vec{q}'_k$ (either the stress vector or the density).

We note that the numerical method presented here describes the fluid flow around a single aggregate but a similar procedure can be employed to determine the flow exterior to several aggregates. Each aggregate then has its own translation and angular velocity vectors, as well as its own force and torque. In that case, it is more natural to set the force and torque on each particle, using equations (17) and (18) or equations (21) and (22), and then solve for the translation and angular velocities, adding two vector equations per aggregate to the linear system.

We now discuss specific features of the single- and double-layer potential methods. For the single-layer potential, we have $\bar{\bar{J}}(\vec{x}', \vec{x}'_k) = \bar{\bar{G}}(\vec{x}', \vec{x}'_k)$, and $\vec{q}'_k = \vec{f}'_k$. In that case, the $3N_f \times 3N_f$ linear system obtained is not full rank. Stress vectors are only found up to a constant multiple of the local normal vectors since a stress vector given by a constant multiple of the local normals results in a zero velocity at the interface and a zero net force and torque. To obtain a unique solution, we add an equation enforcing that

$$\sum_{k=1}^{N_f} \vec{f}'_k \cdot \hat{n}_k = 0, \tag{25}$$

where $\hat{n}_k$ is the outer normal on each face. The resulting $(3N_f + 1) \times 3N_f$ system has a unique solution vector $\vec{f}'_k$.

For the double-layer potential, the unknown density, $\vec{\psi}'_k$, is found using the same discretization (24) applied to equation (20), resulting in a system with no rank deficiency. However, the values of the total force and torque terms must be solved for simultaneously with the unknown density, resulting in a slightly larger system of size $3(N_f + 2) \times 3(N_f + 2)$. These additional equations, (21) and (22), are discretized as,

$$0 \;=\; \int_{S'} \vec{\psi}'(\vec{x}')\, dS'(\vec{x}') - \vec{F}' \;=\; A' \sum_{k=1}^{N_f} \vec{\psi}'_k - \vec{F}', \tag{26}$$

$$0 \;=\; \int_{S'} \vec{\psi}'(\vec{x}') \cdot (\bar{\bar{\epsilon}} \cdot \vec{x}')\, dS'(\vec{x}') - \vec{Q}' \;=\; A' \sum_{k=1}^{N_f} \vec{\psi}'_k \cdot \bar{\bar{\epsilon}} \cdot \vec{x}'_k - \vec{Q}' \tag{27}$$

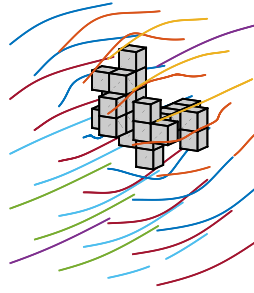where $A' = 4$ is the non-dimensional area of each square.

Figure 5: Sample streamlines of flow past a 20-cube aggregate. The aggregate is assumed to move horizontally, into the page and to the right.

In Fig. 5, we present sample streamlines computed with this numerical method. Here, we show results obtained with the single-layer potential method where the aggregate is assumed to move horizontally with $\vec{U}'_a = (1, 0, 0)$ and $\vec{\Omega}' = (0, 0, 0)$. The double-layer potential would give results that are visually identical. The streamlines were obtained by performing a second order Runge-Kutta time integration once the velocity was computed. The streamlines, computed in the frame of reference of the aggregate, can be seen to be deflected by the object, with weaker deflections further away from the aggregate.

4.1 Validation and Comparison

We proceed to validate and compare our implementation of the single and double-layer approaches. Although the single-layer approach is somewhat simpler to implement, it has been found to yield linear systems with larger condition numbers when integrated using boundary element methods, though with seemingly little impact on its accuracy [47, 41]. We consider a simple system where resolution may easily be varied and compute the flow around a single large cube, subdivided into smaller collated cubes, as shown in Fig. 6. We define $\Delta x = 2/N_x$, where N_x is the number of cubes in each linear dimension, and increase the resolution by increasing N_x. The prescribed translation and angular velocities are kept constant at $\vec{U}'_a = (0, 0, -1)$ and $\vec{\Omega}' = (0, 0, 0)$, respectively. We then compute and compare the total force and torque on the cube.

In Fig. 7(a), we present the non-dimensional drag, D', the z'-component of the total force on the cube,

$$D' = -\vec{F}' \cdot \frac{\vec{U}_a}{||\vec{U}_a||} = \vec{F}' \cdot \hat{k} = \frac{\vec{F} \cdot \hat{k}}{\mu U_s L}, \tag{28}$$
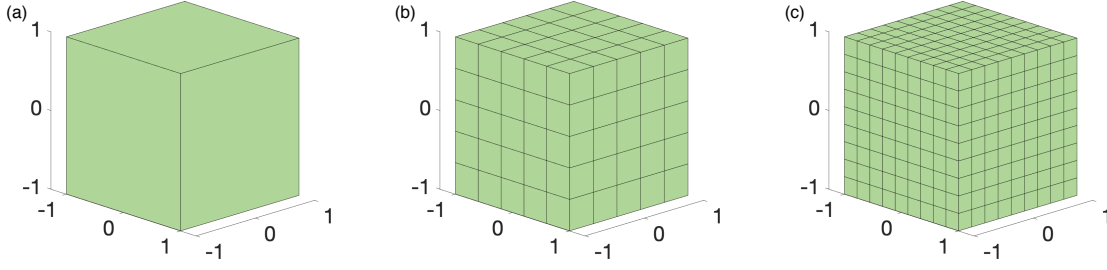
11

Figure 6: Cubes of various resolutions used for validation. All three cubes have the same volume and contain (a) 1 interior cube with length $\Delta x = 2$ (b) $5^3 = 125$ interior cubes with length $\Delta x = 2/5$, and (c) $9^3 = 729$ interior cubes with length $\Delta x = 2/9$.
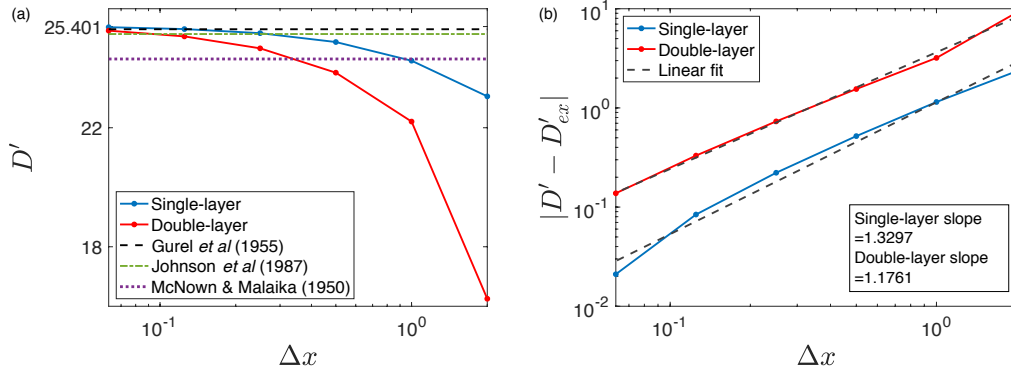

Figure 7: (a) Drag on a cube as a function of Δx for both the single- and double-layer methods. (b) Error of the drag as Δx is varied, shown on a loglog scale. Dashed lines are linear fits to the data. The error is computed by taking the difference between the limit shown in (a), $D'_{ex} = 25.401$, and drag values, D', when $\Delta x = 2, 1, 0.5, 0.25, 0.125,$ and 0.0625.

as computed by both methods, using equations (17) and (21), for various resolutions. We first observe that both methods converge to the same limit value of $D' \approx 25.401$ as we decrease Δx. These results agree very well with the observations of Gurel *et al.* [48] who found a drag of 25.311, and with the empirical relation proposed by Johnson *et al.* [49], which yields a drag of 25.150. Values given in earlier literature are similar but somewhat smaller, with McNown & Malaika [50] reporting a drag of 24.311. These literature values are also plotted in Fig. 7(a).

Fig. 7(b) presents the error relative to the limit value of $D'_{ex} = 25.401$ for both methods. We notice that the convergence rate is similar in both methods, showing a convergence rate slightly higher than one. Typically, one expects to observe a quadratic order of convergence using the mid-point integration rule. However, the order of convergence is likely lower here owing to the presence of edges and corners, which are not treated specially as resolution is increased. The single-layer method is seen to be more accurate than the double-layer method, with an error approximately four times smaller. In other words, a similar degree of accuracy can be obtained with the single-layer method when using a value of Δx four times greater than the double-layer method. The other components of the force acting on the cube as well as the total torque are expected to be exactly zero because of the symmetry of the cube. In our computations, the torque and

12

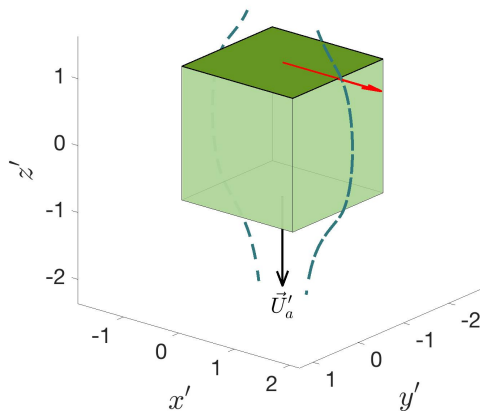the other components of the force never exceed 10^{-10}, as anticipated.

Figure 8: The shaded face is the domain where the stress vector and density shown in Fig. 9 and 10 are computed. The red arrow shows the x-axis used in Fig. 11. Sample streamlines, discussed in Section 4.2, are shown as dashed lines. We also show the translation vector, $\vec{U}'_a$.
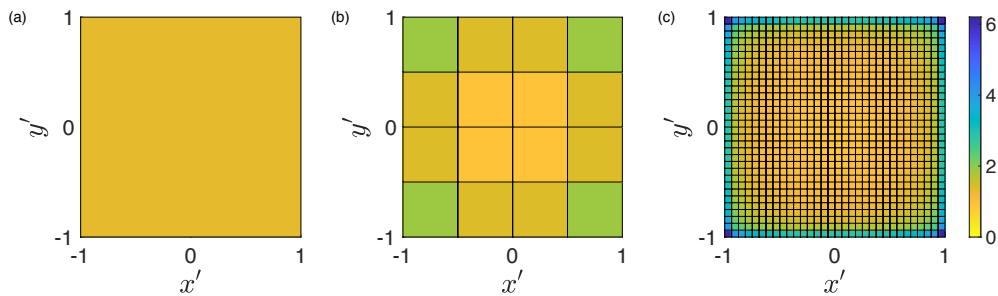

Figure 9: Vertical (z') component of the stress vector, $\vec{f}'$, computed using the single-layer potential shown at $z' = 1$, as illustrated in Fig. 8. The resolution is: (a) $\Delta x = 2$, (b) $\Delta x = 0.5$, and (c) $\Delta x = 0.0625$. The color bar is the same for all three figures.

We now consider point-wise quantities such as the stress vector, density function, and velocity on the surface of the cube and in the fluid exterior to the cube. These quantities are computed in the plane $z' = 1$, which coincides with the face of the cube normal to the incoming flow, as shown in Fig. 8. We show in Fig. 9 and 10 the z'-component of the stress vector, $\vec{f}'$, and of the density, $\vec{\psi}'$, respectively. When varying the resolution of the cube, we obtain N_x^2 different values of the stress vector or density for each side of the cube, each assumed to be constant on a square with side length Δx. Comparing Figs. 9 and 10, it is clear that the stress vector is better approximated by a constant value than the density. As can be seen in both Fig. 9 and 10, convergence is slowest at the edges and even more so at the corners. Despite the rapid variations of the stress vector and density at the corners, the drag is seen to converge with increased resolution, see Fig. 7, though perhaps with a slower order of convergence than would be expected from a mid-point rule. The
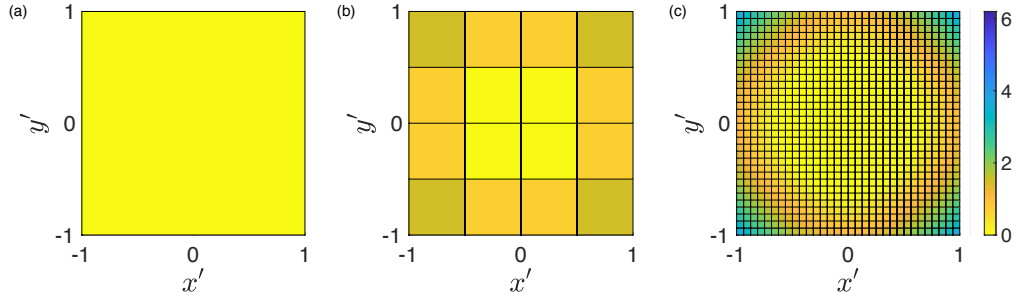
13

Figure 10: Vertical (z') component of the density, $\vec{\psi}'$, computed using the double-layer potential, shown at $z' = 1$, as illustrated in Fig. 8. The resolution is: (a) $\Delta x = 2$, (b) $\Delta x = 0.5$, and (c) $\Delta x = 0.0625$. The color bar is the same for all three figures and the same as in Fig. 9.

single-layer potential approach thus provides a good approximation of the total drag even at low resolution. In contrast, the double-layer potential method finds a density that is varying to a greater extent over the face of the higher-resolution cube, making low resolution estimates less accurate. On the other hand, the variations near the corners are smoother, which could make this method a better choice if one were focusing on the behavior at the edges or corners. These observations are consistent with the single-layer approach resulting in more accurate computations of the drag than the double-layer approach when using the same resolution.
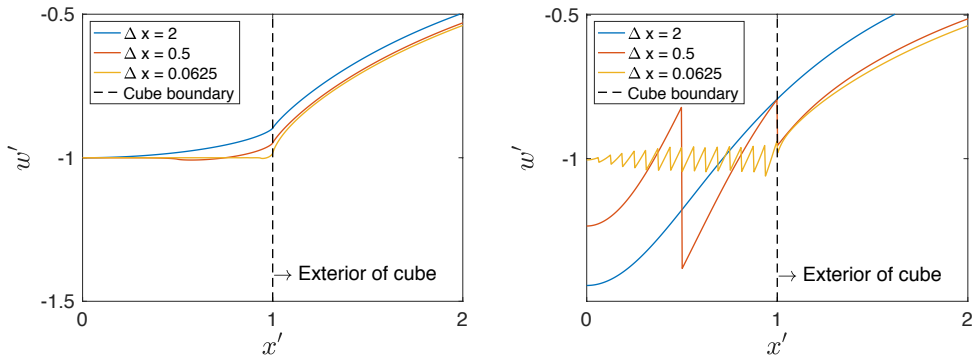

Figure 11: Vertical (z') component of the velocity, denoted by w', along the line $(x', 0, 1)$ as illustrated in Fig. 8. We show three different resolutions for the (a) single-layer method and (b) double-layer method.

We next present analysis of the $z'-$component of the velocity, w', when the cube has the same translation velocity, $\vec{U}'_a = (0, 0, -1)$. In Fig. 11, we present this velocity along the line $(x', 0, 1)$, shown in Fig. 8 as the red arrow, as we vary the resolution of the cube for both the single-layer and double-layer approaches. When using the single-layer potential, we compute the velocity for all points using equation (16). For the double-layer potential approach, we compute the velocity at points on the surface of the cube using equation (20) and at points in the fluid exterior to the cube using equation (19). In Fig. 11, dashed lines represent the edge of the cube, i.e. points $x' \in [0, 1]$ are on the cube surface and points $x' \in (1, 2]$ are exterior to the cube. Since we impose the translation velocity, $\vec{U}'_a$ at the center of each square, we expect that $w' = -1$ for $x' \in [0, 1]$. We observe that on the cube surface, the single-layer method, shown in Fig. 11(a), results

14

in smoother velocities than the double-layer method, shown in Fig. 11(b). In Fig. 11(a), as Δx decreases, the velocities on the surface of the cube are converging to -1. The velocity on the edge of the surface, at $x' = 1$, does not agree exactly with the expected value, though it approaches -1 as Δx decreases. On the other hand, the double-layer approach has discontinuous oscillations of the velocity on the surface. This is due to our assumption of locally constant, and thus discontinuous, $\vec{\psi}'$, which directly affects the velocity in equation (20). The oscillations decrease in amplitude as Δx decreases, and the velocity exterior to the cube is smooth. The discrepancy with the expected velocity at the edge of the cube, $x' = 1$, is greater than for the single-layer approach.
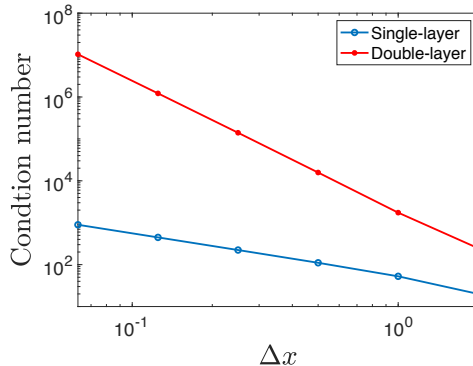

Figure 12: Comparison of the condition number for the linear system of both the single-layer and double-layer methods as the resolution of the cube is varied.

We conclude the comparison of the two methods by considering their computational complexity. It has been observed that Fredholm integral equations of the first kind, such as that associated with the single-layer potential, often lead to ill-posed numerical methods when the surface integral is discretized [51, 52]. The main challenge is dealing with the singularity of the the integral kernel. However, in our method, we compute the surface integrals analytically over each square, so that the kernel singularities are integrated exactly. In addition, we constrain the system to have a unique solution through equation (25). We compare the condition number of the linear system of each of our two methods for various resolutions in Fig. 12. We find that the condition number of the single-layer method is approximately inversely proportional to Δx. On the other hand, the condition number of the double-layer method is approximately inversely proportional to $(\Delta x)^3$, and is thus much greater.

Based on our findings of more accurate drag, smoother and more accurate velocity, and smaller condition number, we conclude that the single-layer potential approach is more appropriate to model flow around aggregates made of cubic particles. In the remainder of this paper, we therefore present results obtained using the single-layer approach.

4.2   Streamlines

To gain a better understanding of the flow around a cube, we present the streamlines generated when $\vec{U}'_a = (0, 0, -1)$. We show the streamlines around the cube in the frame of reference of the cube for $y' = 0$ in Fig. 13 (see Fig. 8 for the exact location of the face and sample streamlines). To compute the streamlines, we first obtain the values of stress vector, $\vec{f}'(\vec{x}'_s)$, on each square face of the cube using equation (16). We then chose initial positions below the cube and use a second order Runge-Kutta method to advance the positions in time using the corresponding velocities computed using equation (16) at each position. We compare the

15

streamlines with four different resolutions of the cube; $\Delta x = 2, 1, 0.5$, and 0.25. For the cube with $\Delta x = 2$, streamlines are seen to enter the interior of the cube. As we increase the resolution, the streamlines remain exterior to the cube. Moreover, higher resolutions result in streamlines following the cube boundary more accurately, showing the convergence of the method.
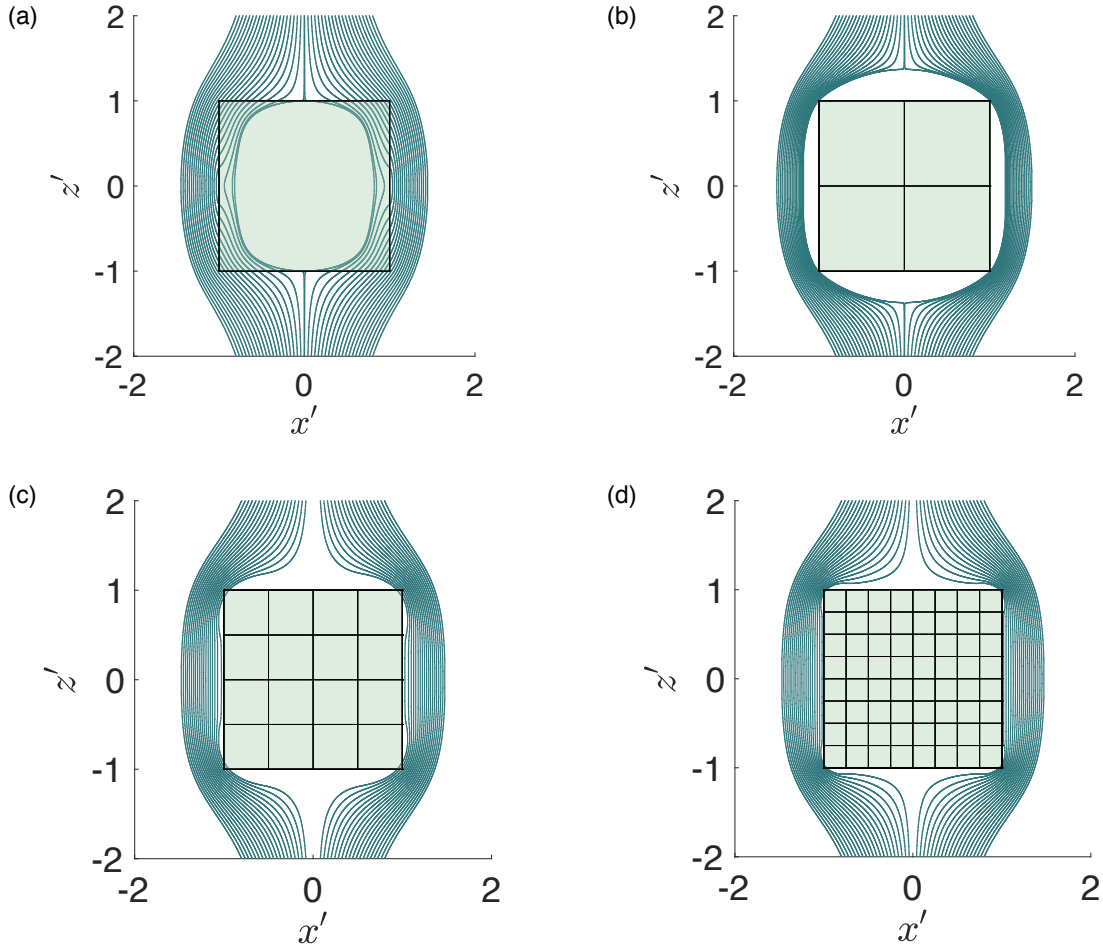

Figure 13: Streamlines around a cube with varying resolution moving in the $z'-$direction. The resolution is: (a) $\Delta x = 2$, (b) $\Delta x = 1$, (c) $\Delta x = 0.5$, and (d) $\Delta x = 0.25$.

5   Results: Forces on Aggregates Subject to a Background Flow

In this section, we present the response of aggregates when subjected to various flow fields. We consider an aggregate at rest, with boundary condition $\vec{u}' = 0$ on the surface of the aggregate, subject to a background flow. Three common background flows are considered, which can be combined to provide an approximation of any general flow to first order in space: $\vec{U}'_{bg}(\vec{x}) = -\vec{U}'_a - \vec{\Omega}' \times \vec{x}' + \bar{\bar{M}}' \cdot \vec{x}'$, the primes indicating dimensionless quantities as above. Here, $-\vec{U}'_a$ is the translation velocity of the flow past an aggregate or

16

equivalently when changing frame of reference, a constant settling velocity $\vec{U}_a'$ of the aggregate in a fluid at rest. Similarly, $-\vec{\Omega}'$ is the constant angular velocity of a rotating flow around an aggregate, or equivalently when changing frame of reference, the constant angular velocity of a rotating aggregate in a fluid at rest. Lastly, $\bar{\bar{M}}'$ is a traceless, symmetric tensor that induces a straining flow around the aggregate. In all three cases, to solve for the response of the aggregates, we decompose the fluid velocity as $\vec{u}' = \vec{U}_{bg}' + \vec{U}_c'$, where the correction velocity, $\vec{U}_c'$, decays to zero at infinity and satisfies $\vec{U}_c' = -\vec{U}_{bg}'$ on the surface of the aggregate. Using this formulation allows for this correction to be computed via the single-layer potential boundary integral as described above in Sections 3 and 4.
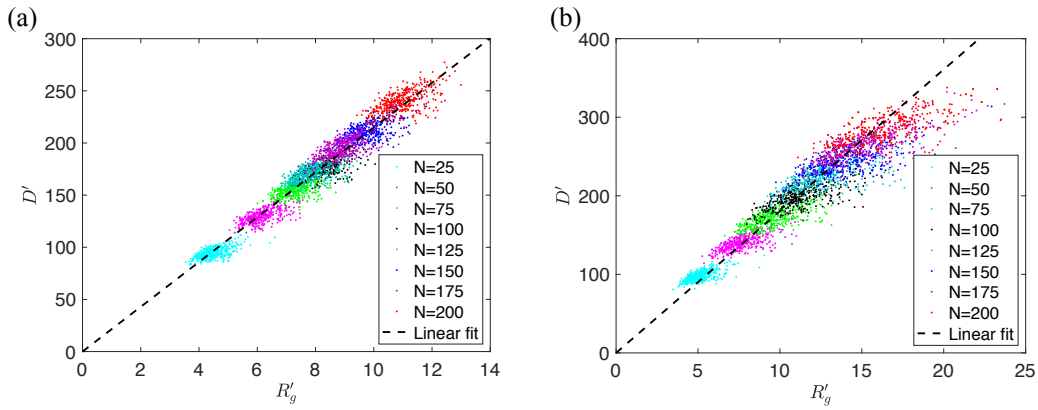
5.1 Translation Flow

Figure 14: Non-dimensional drag of aggregates in a constant flow, $\vec{U}_{bg}' = -\vec{U}_a' = (0,0,1)$, as a function of gyration radius R_g' for aggregates of different sizes, N. We present in (a) the drag of individually-added-aggregates (IAA) and in (b) the drag of cluster-cluster-aggregates (CCA). The dashed lines are least-square linear fits: in (a) $D' = 21.47 R_g'$ and in (b) $D' = 18.04 R_g'$.

We first consider a constant background velocity, $\vec{U}_{bg}'(\vec{x}') = -\vec{U}_a' = (0,0,1)$. In Fig. 14 we present the non-dimensional drag on the aggregate, D', as defined in equation (28), as a function of the non-dimensional gyration radius, R_g', of each aggregate. We show in Fig. 14(a) the drag on aggregates formed by individual random walkers (IAA), and in Fig. 14(b) the drag on aggregates formed by cluster aggregation (CCA). Recall that aggregates formed by individually-added random walkers tend to be more compact. The drag appears to scale linearly with the gyration radius for both types of aggregates, as would be expected from dimensional considerations for the proper measure of the size of an aggregate. Note that for all the fits presented in this section, we compute the coefficient of determination, $\mathbf{R}^2$, using either the gyration or maximum radius as an independent variable, to assess how closely each model fits the data.

To verify this linear relationship between the drag and the gyration radius, we found the slope of D' as a function of R_g' on a loglog plot, giving the best exponent, α, in the relation $D' \sim (R_g')^\alpha$. This confirmed that a linear fit was optimal for IAA, finding $\alpha = 1.00$, and found a somewhat smaller exponent for CCA, with $\alpha = 0.85$. Assuming a linear relation, we find for individual aggregation (IAA) that a least-square fit has a slope of 21.47 with a coefficient of determination of $\mathbf{R}^2 = 0.95$ (Fig. 14(a)) For cluster aggregation (CCA), we find a best-fit line with slope 18.04, and a corresponding coefficient of determination of $\mathbf{R}^2 = 0.86$ (Fig. 14(b)).

These results are consistent with experimental results which showed a linear relationship between the drag

on an aggregate and the square root of A'_p, the two-dimensional projected area of the aggregate [21]. In addition to computing the drag as a function of the gyration radius, we computed the drag of aggregates as a function of their projected area. We found that A'_p was not as good predictor of the drag experienced by the aggregate. In particular, for aggregates containing a fixed number of cubes, we observed no correlation between the projected area and the drag experienced by the aggregate. A similar observation holds for the torque and straining force discussed below, and as a result, we choose to present all of our results in terms of either the maximum or gyration radius.
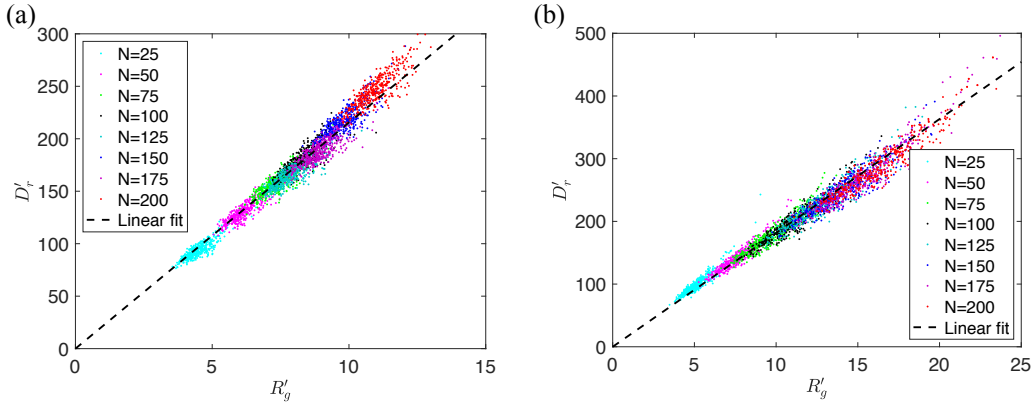

Figure 15: Rescaled non-dimensional drag, D'_r, as a function of gyration radius R'_g for (a) individually-added aggregates (IAA) and for (b) cluster-cluster-aggregates (CCA). The rescaled drag, D'_r, is defined in equation (29) and the fits to the data, plotted as dashed lines, are given in equation (30) for (a) and in equation (31) for (b).

Although the relationship between the drag and gyration radius is nearly linear, there appears to be further structure in the data obtained, as is particularly visible for CCA in Fig. 14(b). For an aggregate composed of a fixed number of cubes, N, the drag increases linearly with aggregate size, but at a slower rate than when N is also allowed to vary. To better characterize this dependency, we introduce a rescaled non-dimensional drag that takes into account the difference between the gyration radius of a given aggregate and the mean gyration radius of all aggregates with the same number of cubes. We denote the average gyration radius for aggregates of N cubes as $\bar{R}'_g(N)$. Similarly, we define an average maximum radius for aggregates made of N cubes as $\bar{R}'_m(N)$. We may then define the departure from these average value as

$$\sigma_g = \frac{R'_g - \bar{R}'_g}{\bar{R}'_g} \quad \text{and} \quad \sigma_m = \frac{R'_m - \bar{R}'_m}{\bar{R}'_m}.$$

These measures are positive when the aggregate is more spread out than the mean aggregate size and negative when the aggregate is more compact than the mean. We use these measures to define a rescaled drag that accounts for the variability in the aggregate radius as

$$D'_r = \frac{D'}{1 + \gamma \sigma_g}, \tag{29}$$

where γ is an empirical parameter that we fit based on the data. To optimize the collapse, we choose γ to maximize the correlation coefficient between the rescaled drag and the gyration radius.

As seen in Fig. 15 the data collapses better. For IAA, we find $\gamma = -0.43$, with a best-fit line of $D'_r = 21.55 R'_g$, which improves the coefficient of determination to 0.97, which is a relatively small gain as the data was

18

already nearly linear. This negative value of γ indicates that less compact aggregates experience more drag than more compact aggregates when composed of the same number of cubes. The drag is thus well described by

$$D' = 21.55 \left(1 - 0.43 \frac{R'_g - \bar{R}'_g}{\bar{R}'_g} \right) R'_g . \tag{30}$$

where the mean gyration radius is $\bar{R}'_g = 1.32 N^{0.39}$, as described in Section 3. For CCA, the same procedure yielded $\gamma = -0.64$, and the resulting collapse is shown in Fig. 15(b). The rescaled drag follows a much improved linear relationship as a function of the gyration radius, with a slope of 18.16 and a coefficient of determination of $\mathbf{R}^2 = 0.97$. A complete description of the drag for CCA is thus

$$D' = 18.16 \left(1 - 0.64 \frac{R'_g - \bar{R}'_g}{\bar{R}'_g} \right) R'_g \tag{31}$$

where the mean gyration radius is $\bar{R}'_g = 0.85 N^{0.56}$. A similar dependence was found when replacing the gyration radius with the maximum radius or the square root of the projected area. However, the coefficients of determination were then lower, by approximately %, and the best fit exponents, α, were lower for the gyration radius and further from one for the projected area (lower for IAA, higher for CCA). This indicates that the gyration radius is a better descriptor of the size of an aggregate when considering the drag.
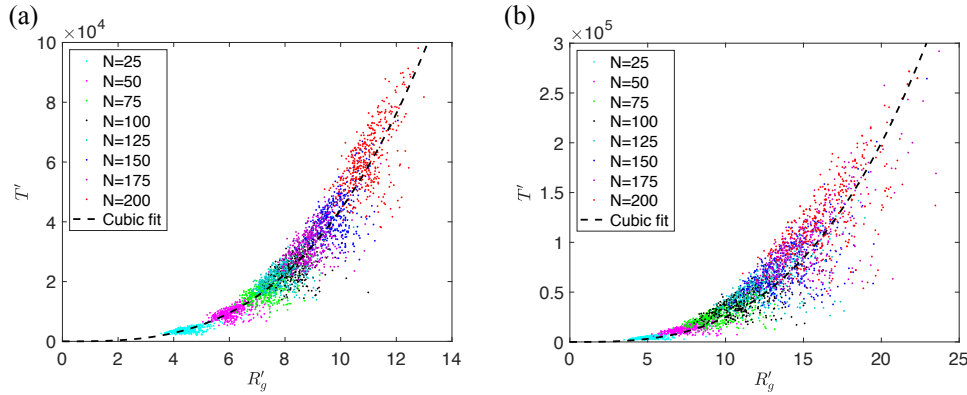
5.2 Rotating flow

Figure 16: Non-dimensional torque, T', defined in equation (32), as a function of gyration radius, R'_g, for aggregates composed of a varying number of cubes, N. In (a) individually-added-aggregates (IAA) are presented and in (b) cluster-cluster-aggregates (CCA) are presented. The dashed lines are least-square cubic fits: in (a) $T' = 44.12(R'_g)^3$ and in (b) $T' = 24.98(R'_g)^3$.

In Fig. 16, we present the non-dimensional torque as a function of gyration radius for aggregates subject to a rotating background flow, $\vec{U}'_{bg}(\vec{x}') = -\vec{\Omega}' \times \vec{x}'$. We present only the component of the torque parallel to $\vec{\Omega}'$, as the other two components both average to zero. This component, T', is non-dimensionalized using the angular velocity,

$$T' = -\vec{Q}' \cdot \frac{\vec{\Omega}'}{||\vec{\Omega}'||} \quad \text{and} \quad \vec{Q}' = \frac{\vec{Q}}{\mu ||\vec{\Omega}|| L^3} \tag{32}$$

19

Here, we expect a cubic dependence of the torque on a properly chosen measure of the size of the aggregate, in contrast to the linear dependence of the drag as described in Section 5.1. This is because computing a torque rather than a force increases the order of dependence on the gyration radius by one. In addition, this calculation is based on an imposed angular velocity, $\vec{\Omega}'$, rather than a translation velocity, which also increases the order of the dependence on the gyration radius by one. We verified that a cubic fit was the most appropriate by finding the slope on a loglog plot of the torque as a function of gyration radius, yielding the best exponent α in the relation $T' \sim (R'_g)^\alpha$. This confirmed that a cubic fit was optimal for IAA, with $\alpha = 3.00$, and again we observed a somewhat smaller exponent for CCA, with $\alpha = 2.68$, indicating that the torque of CCA shows a slower average growth. Furthermore, for CCA, as can be seen in Fig. 16(b), there is noticeably more variability. Assuming a cubic fit, we find for the IAA a least-square fit of $T' = 44.12(R'_g)^3$ with coefficient of determination $\mathbf{R}^2 = 0.91$ and for the CCA a least-square fit of $T' = 24.98(R'_g)^3$ with coefficient of determination $\mathbf{R}^2 = 0.81$. Here too, a similar dependence was found when replacing the gyration radius with the maximum radius or projected area, though again with smaller coefficients of determination and best fit exponents further from three as expected from dimensional analysis, so that the gyration radius is also more useful descriptor of the size of an aggregate when studying the torque.
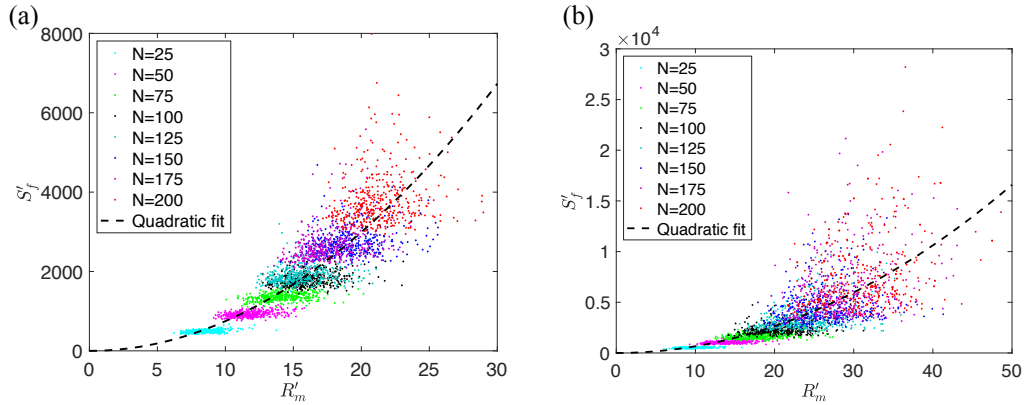
5.3 Extensional flow

Figure 17: Non-dimensional straining force, S'_f, defined using equations (33) and (34), as a function of the maximum radius, R'_m, for aggregates of different sizes N. In (a) individually-added-aggregates (IAA) and in (b) cluster-cluster-aggregates (CCA) are presented. The dashed lines are least-square quadratic fits: in (a) for IAA, $S'_f = 7.48(R'_m)^2$ and in (b) for CCA, $S'_f = 6.64(R'_m)^2$.

We now consider the response of an aggregate to an extensional flow, $\vec{U}'_{bg}(\vec{x}') = \bar{\bar{M}}' \cdot \vec{x}'$. In such a background flow, for an object with no preferred orientation, the drag and torque both average to zero. However, the aggregate will be under effective tension or compression, an effect that could lead to rupture. Quantifying these forces is relevant to the formation and breakup of marine aggregates. We therefore define a straining force vector, $\vec{E}$, that quantifies this effect. We non-dimensionalize this force using the largest eigenvalue in magnitude of the matrix $\bar{\bar{M}}$ which we denote by $|\lambda|$, and obtain

$$\vec{E}' = \frac{\vec{E}}{\mu|\lambda|L^2}. \tag{33}$$

The straining force may be decomposed as $\vec{E}' = E'_1\hat{v}_1 + E'_2\hat{v}_2 + E'_3\hat{v}_3$, where the $\hat{v}_i$ are the real, orthonormal eigenvectors in the spectral decomposition of $\bar{\bar{M}}'$, which is always possible since $\bar{\bar{M}}'$ is symmetric. The

components of $\vec{E}'$ are then defined as

$$E'_i = \frac{1}{2} \left(\int_{S'} |\vec{f}' \cdot \hat{v}_i| \, dS' - \left| \int_{S'} \vec{f}' \, dS' \right| \cdot \hat{v}_i \right), \tag{34}$$

where $\vec{f}' \cdot \hat{v}_i$ is the projection of the stress vector in the direction of the eigenvector $\hat{v}_i$. This straining force is a measure of how much stress imposed in one direction is also applied in the opposite direction resulting in a strain on the aggregate. The factor of $1/2$ accounts for the double counting of the tensile or compressive forces when integrating the stress vector in the direction of, and opposite to, the vector $\hat{v}_i$. We have subtracted the component of the net force in each direction to obtain a straining force that is independent of the net force on the object. In the results shown in this section, we consider two-dimensional extensional flows, for which the eigenvalues are -1 in the x'-direction, 1 in the y'-direction, and 0 in the z'-direction. We present the component of the straining force in the y'-direction, denoted as S'_f.

For the straining force, dimensional considerations lead us to expect a quadratic dependence on an appropriate measure of the aggregate's size. However, we found that the slope of the straining force as a function of gyration radius on a loglog plot, giving the exponent α in the relation $S'_f \sim (R_g)'^\alpha$, yielded values greater than two for both IAA and CCA, with exponents of 2.1 and 2.2, respectively. In contrast, using the maximum radius as a measure of the aggregate's size resulted in a dependence that was much closer to being quadratic, with best fits on the growth exponent giving $S'_f \sim (R'_m)^{1.98}$ for IAA and $S'_f \sim (R'_m)^{2.01}$ for CCA. We therefore present the data as a function of the maximum radius rather than the gyration radius, as R'_m appears to be a better predictor of the straining force. In Fig. 17, we present S'_f for aggregates of different sizes as a function of the maximum radius, R'_m. The dashed lines in Fig. 17 are quadratic fits to the data as a function of maximum radius and we find best fits of $S'_f = 7.48(R'_m)^2$ for IAA with coefficient of determination of $\mathbf{R}^2 = 0.74$, and $S'_f = 6.64(R'_m)^2$ with coefficient of determination of $\mathbf{R}^2 = 0.56$ for CCA. For both IAA and CCA, we observe that if N is held constant and the maximum radius varied, the growth of the straining force seems to be significantly slower than quadratic. This once again suggests a rescaling as in Section 5.1.
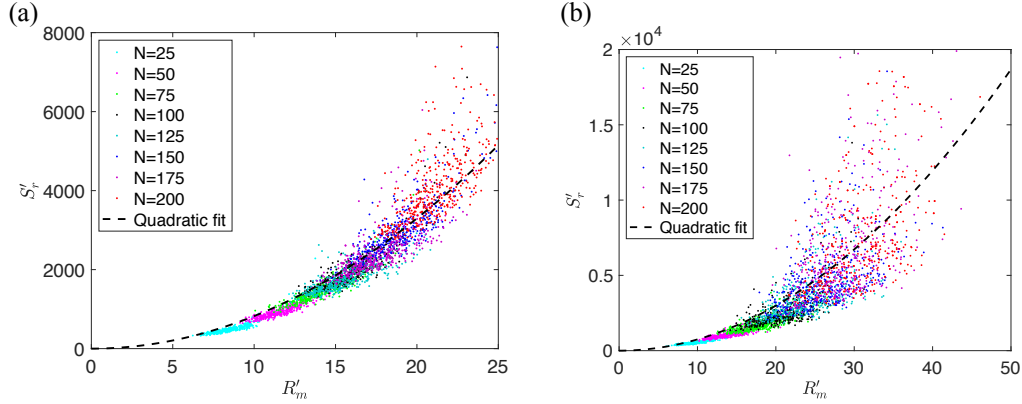
Figure 18: Rescaled non-dimensional straining force, S'_r, as a function of maximum radius R'_m for aggregates of different sizes N. In (a) individually-added-aggregates (IAA) and in (b) cluster-cluster-aggregates (CCA) are presented. The dashed lines are least-square quadratic fits: in (a) for IAA, $S'_r = 8.24(R'_m)^2$, in (b) for CCA, $S'_r = 7.47(R'_m)^2$.

To rescale the straining force, we define

$$S'_r = \frac{S'_f}{1 + \gamma \sigma_m},$$

21

with σ_m defined above as the non-dimensional deviation from the average maximum radius for aggregates of the same size. This rescaled force yields a better collapse of the data, as can be seen in Fig. 18, particularly for IAA. We found that the best rescaling value was $\gamma = -1.32$ for IAA and $\gamma = -0.92$ for CCA. In the CCA case the resulting data appears to grow slightly faster than quadratic. Nonetheless, it is possible to fit a quadratic to the rescaled drag, and doing so yields $S'_r = 8.24R_m^2$ with coefficient of determination $\mathbf{R}^2 = 0.89$ for IAA and $S'_r = 7.47R_m^2$ with coefficient of determination $\mathbf{R}^2 = 0.63$ for CCA.

We note that the straining force, even when rescaled, exhibits a large amount of scatter compared to the torque and drag, particularly for CCA, which tend to have more elongated aggregates. Observing individual aggregates of similar size but different straining forces reveals that the straining force is particularly sensitive to the orientation of an aggregate. The scatter is thus largely due to this sensitivity, as the same aggregate oriented differently can experience a significantly different straining force.

6 Discussion

The results presented above all use a resolution of $\Delta x = 2$, which corresponds to using aggregates made of cubes of non-dimensional side length 2, not further refined. To assess the accuracy of results with this resolution, we considered 16 different aggregates made of 100 cubes of side length 2 and refined the resolution to use $\Delta x = 2, 1$, and $2/3$, thus increasing the number of cubes from 100 to 800 and 2700 while maintaining the aggregate shape. Both the drag and torque were seen to converge as resolution was increased. The coarsest resolution, used in the section above, yielded results that were less than 2% away from the more highly resolved results for the drag, and less than 5% away for the torque (we found for similar sampling that the extensional force behaved in a manner between that of the drag and torque). For comparison, the standard deviation of the drag and torque of the samples considered was approximately three times as large for all resolution studied. The variability between aggregates of a given size thus far exceeds the error due to a coarse resolution. Further, we performed a similar study on aggregates of various sizes and found that effects of a coarse resolution decreased as the size of the aggregate increased. The data we present is for aggregates of size ranging from 25 to 200 cubes with $\Delta x = 2$, and is therefore sufficiently accurate to allow a meaningful quantification of the drag, extensional force, and torque.

To put the results for aggregates obtained in section 5 into context, we compare them to the well-known corresponding results for a sphere [53]. The gyration radius of a sphere of radius R_s is $R_g = \sqrt{2/5}R_s$ and thus the Stokes hydrodynamic force acting on a sphere is $\vec{F} = 6\pi\mu\vec{U}_aR_s \approx 29.8\mu\vec{U}_aR_g$. Also, the torque on a rotating sphere is $\vec{Q} = 8\pi\mu\vec{\Omega}R_s^3 \approx 99.35\mu\vec{\Omega}R_g^3$. For a sphere in an extensional flow, the exact solution of the straining force for the flow satisfying $\vec{U}_{bg} = \bar{\bar{M}} \cdot \vec{x}$ at infinity and $\vec{U}_{bg} = 0$ on the surface of the sphere is known [53]. The details of the computation of the corresponding straining force are given in the appendix. We find that for a matrix $\bar{\bar{M}}$ with unit eigenvector $\hat{v}_i$ and corresponding eigenvalue λ_i, the straining force is

$$E_i = \frac{1}{2}\int_S |\vec{f} \cdot \hat{v}_i|\, dS = 5\pi\mu R_s^2\lambda_i \approx 15.7\mu R_m^2\lambda_i,$$

where we used that the maximum radius R_m of a sphere is simply its usual radius R_s and that a sphere in an extensional flow experiences no net force.

Our results from Section 5, and the corresponding results for a sphere, are summarized in Table 1. We first note that the hydrodynamic force acting on translating aggregates is significantly less than that acting on a translating sphere of the same gyration radius. This is presumably because the aggregates are not densely filled, and thus allow some flow to effectively go through them. For the same reason, the force on the more compact IAA is also greater than that on the less compact CCA. Similarly, the coefficients of the torque for both types of rotating aggregates are less than those of the corresponding rotating sphere. This

is, once again, because less compact structures encounter less torque from the fluid when rotating. Further, a similar observation also holds for the straining force when in an extensional flow, where denser structures are subject to a larger straining force for an equivalent radius.

	Sphere	IAA	CCA
Force $(-\vec{F})$	$29.8\mu\vec{U}_a R_g$	$21.47\mu\vec{U}_a R_g$	$18.04\mu\vec{U}_a R_g$
Rescaled Force $(-\vec{F}_r)$	N/A	$21.55(1-0.43\sigma_g)\mu\vec{U}_a R_g$	$18.16(1-0.64\sigma_g)\mu\vec{U}_a R_g$
Torque $(-\vec{Q})$	$99.35\mu\vec{\Omega}R_g^3$	$44.12\mu\vec{\Omega}R_g^3$	$24.98\mu\vec{\Omega}R_g^3$
Straining Force $(\vec{E})$	$15.7\mu R_m^2|\lambda|\hat{v}$	$7.48\mu R_m^2|\lambda|\hat{v}$	$6.64\mu R_m^2|\lambda|\hat{v}$
Rescaled Strain. For. (S_r)	N/A	$8.24(1-1.32\sigma_m)\mu|\lambda|R_m^2$	$7.47(1-0.92\sigma_m)\mu|\lambda|R_m^2$

Table 1: Summary of results from section 5 compared to corresponding results for a sphere.

We may use our results to define a hydrodynamic radius, R_h, as the radius of a sphere subject to similar forces or torque as a given aggregate. The exact hydrodynamic radius varies if we consider the force, torque, or straining force in their corresponding flows. On average, we find that the hydrodynamic radius obtained considering forces and torques was approximately $R_h \approx 1.15R_g$ for individually-added aggregates, and $R_h \approx 1.01R_g$ for cluster-cluster aggregates. These results are consistent, though with a smaller coefficient, with results found in terms of the maximum radius and based on the drag alone by Zhang and Zhang [27]. It should be noted that corresponding spheres would also have a far larger volume, as volume scales like $V \sim R_g^3$ for spheres, while the volume of individually formed aggregates scales as $V \sim R_g^{2.57}$ and that formed by cluster aggregation scales as $V \sim R_g^{1.79}$.

As stated in the introduction, many models make use of the settling speeds of aggregates. We can use our computed force to obtain a settling speed for an aggregate with given departure from the mean radius of aggregates of similar size, σ_g, and gyration radius R_g. To do so, we match the hydrodynamic force with the buoyancy force, $\vec{F}_b = \vec{g}V\Delta\rho$. Here $\Delta\rho$ is the density difference between the aggregate and the external fluid and $V = 8L^3N$ is the aggregate volume, with L the half-width of the cubes forming the aggregates and N the number of cubes within an aggregate. Depending on the aggregate formation mechanism, the number of cubes will scale differently with the gyration radius. For IAA, we found in Section 2 that $N = 0.24(R_g')^{2.56}$ and for CCA, we found that $N = 1.34(R_g')^{1.79}$. Using equation (30) for IAA, and equation (31) for CCA, we may solve for the Stokes settling speed of aggregates. We thus find, for IAA

$$\vec{U}_a = 0.19 \left(\frac{\vec{g}\Delta\rho L^{0.44}R_g^{1.56}}{\mu} \right) \left(\frac{1}{1-0.43\sigma_g} \right), \tag{35}$$

and for CCA

$$\vec{U}_a = 0.58 \left(\frac{\vec{g}\Delta\rho L^{1.21}R_g^{0.79}}{\mu} \right) \left(\frac{1}{1-0.64\sigma_g} \right). \tag{36}$$

For comparison, the settling speed of a sphere in terms of its gyration radius is

$$\vec{U}_a = \frac{5}{9} \left(\frac{\vec{g}\Delta\rho R_g^2}{\mu} \right). \tag{37}$$

These results are consistent with measurements that found that aggregates of fractal dimension close to three, more similar to IAA, had a settling speed of aggregates slower than predictions based on the settling speed of a corresponding sphere [4].

We note that the increase of the settling speed as a function of aggregate size is slower than for solid objects, particularly for CCA, where the growth only scales as $R_g^{0.79}$. Moreover, we remark that our initial estimate

of the Reynolds number of an aggregate was based on the Stokes settling speed of a sphere, which over-estimates the settling speed of an aggregate. The use of the Stokes equations is therefore appropriate for aggregates with diameter even larger than 1mm as initially argued.

Finally, we note that settling aggregates are generally subject to a non-zero torque and, equivalently, rotating aggregates are subject to a non-zero force. This is a result of the asymmetrical shape of any particular aggregate, which causes aggregates to spin as they settle, or equivalently to settle as they spin. This induced motion has no preferred direction, and so the average over all the aggregates generated here is zero. However, we have computed the standard deviation of the drag of all aggregates subject to an angular velocity $\vec{\Omega}$ and found that it scaled roughly quadratically with the gyration radius. In general then, one finds that a settling aggregate spins at a rate given by a fraction of the ratio of its settling speed over its gyration radius, $||\vec{\Omega}|| \sim ||\vec{U}_a||/R_g$, with the proportionality constant being approximately 0.005 for IAA and 0.013 for CCA.

7 Conclusion

We have developed a novel implementation of boundary integral methods for flow around aggregates composed of cubes. In this case, we found that the single-layer approach was more accurate and therefore used it to study the flow around randomly formed aggregates. We have presented results of the flow around individually-added aggregates and cluster-to-cluster aggregates and characterized the resulting forces on the aggregates. We have identified a suitable length scale to characterize the behavior of fractal aggregates in various contexts. To describe the drag or force, and torque, on an aggregate, the gyration radius, R_g, is the best choice, with respective scalings of $\vec{F} \sim \mu \vec{U}_a R_g$ and $\vec{Q} \sim \mu \vec{\Omega} R_g^3$, as should be expected in Stokes flow. An improved collapse of the drag is possible if we account for an aggregate's departure from its typical size, $\bar{R}_g$, through the factor $\sigma_g = \frac{R_g - \bar{R}_g}{\bar{R}_g}$. The nearly linear relationship between the drag and the gyration radius indicates that the choice of R_g to describe the size of an aggregate is an appropriate one while, for example, the volume-based size $L = V^{1/3}$ would not yield a linear relationship with the drag.

We have also considered the effects of extensional flow on aggregates, an aspect that has been understudied. We introduced a simple characterization of the straining force, $\vec{E}$, on a solid object. We used computations of the straining force to determine that the maximum radius, R_m, is the most appropriate length scale to predict the impact of extensional flow on an aggregate and found that $\vec{E} \sim \mu |\lambda| R_m^2 \hat{v}$. This is particularly relevant when considering aggregate formation and break up. As in the case of the force, an improved collapse of straining force is possible using an aggregate's departure from its typical size, $\sigma_m = \frac{R_m - \bar{R}_m}{\bar{R}_m}$.

Our numerical approach can be directly applied to compute the flow around several particles. We thus plan to use it in future work to conduct a more accurate investigation of aggregate formation. In the present study, as is the case in the vast majority of diffusion-limited aggregation studies, aggregates were formed without factoring in flow dynamics. Our numerical approach allows us to determine dynamically the response of the system when subjected to stochastic forces. Rather than assuming a constant drag and no deformation, we may instead calculate the forces acting on every particle, determine the deformation or potential break-up of the particles by matching the viscous stress with the particle's elastic stress, and determine the aggregates settling velocity as it deforms. Such an approach should provide the most accurate aggregate formation model yet, which in turn will allow for a more accurate characterization of their properties.

Another promising avenue for future work is the incorporation of stratification effects. Marine aggregates typically settle in a water column where the density increases with depth, owing to salinity and temperature variations. Since aggregates are very porous, they are sensitive to stratification [11]. Fluid entrainment and diffusive effects play a role to first stop, and then restart the settling of the porous aggregate [13]. This

process has already been modeled using spherical particles, but how diffusion affects fractal-like aggregates remains unclear. By coupling the current simulations to a concentration field subject to advection-diffusion and tracking its effect on the particle density, one should be able to obtain a simple but improved approximation of the behavior of aggregates settling in a stratified ambient. Our approach may also be extended, though with a significant increase in computational effort, to account for the effects of stratification on the flow itself by adding a volume integral of the concentration to equation (6), thus providing a complete picture of the effects of density stratification.

Acknowledgements
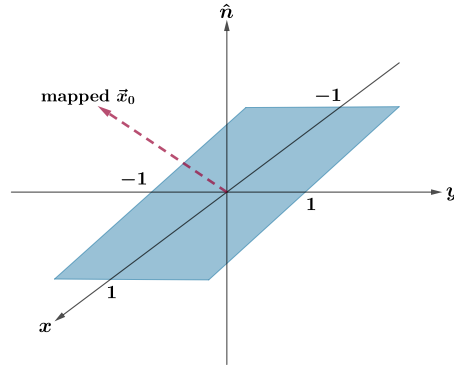
A   Exact Kernel Integration

Figure 19: Schematic of the mapped domain where numerical integration is performed.

When computing the flow around the aggregates, we need to integrate over square surfaces. To integrate over any square face, we first map the square over which we need to integrate to the square $(x, y, 0)$ with $x \in [-1, 1]$ and $y \in [-1, 1]$, as depicted in Fig. (19). The normal to the surface is thus always in the $z-$direction. We may then exactly evaluate all the surface integrals involved in either the single-layer or double-layer potential methods.

A.1   Single-layer potential

In the single-layer potential approach, we need to compute integrals of the form

$$\int_S \left(\frac{\bar{\bar{I}}}{||\vec{x} - \vec{x}_0||} + \frac{(\vec{x} - \vec{x}_0)(\vec{x} - \vec{x}_0)}{||\vec{x} - \vec{x}_0||^3} \right) \mathrm{d}S(\vec{x}) = \int_S \frac{\bar{\bar{I}}}{||\vec{x} - \vec{x}_0||} \mathrm{d}S(\vec{x}) + \int_S \frac{(\vec{x} - \vec{x}_0)(\vec{x} - \vec{x}_0)}{||\vec{x} - \vec{x}_0||^3} \mathrm{d}S(\vec{x}) = I_1 + I_2.$$
(38)

Here, we have that $\vec{x} = (x, y, 0)$ and we write $\vec{x}_0 = (x_0, y_0, z_0)$ and

$$||\vec{x} - \vec{x}_0|| = R(x, y) = \sqrt{(x - x_0)^2 + (y - y_0)^2 + z_0^2}$$

We first consider the case when $x_0 = y_0 = z_0 = 0$, which arises when integrating over a face centered at the point where we are computing the velocity. In that case, we have $R(x, y) = \sqrt{x^2 + y^2}$. We find for the diagonal terms of I_1

$$\int_{-1}^{1} \int_{-1}^{1} \frac{1}{\sqrt{x^2 + y^2}} \, \mathrm{d}x\mathrm{d}y = 8 \arcsinh(1) \tag{39}$$

and all the non-diagonal terms are zero.

Away from the singularity, we can generally find antiderivatives, computed using Mathematica. For the integral I_1, we have

$$\int_S \frac{1}{||\vec{x} - \vec{x}_0||} \mathrm{d}S(\vec{x}) = \int_{-1}^{1} \int_{-1}^{1} \frac{1}{R(x, y)} \, \mathrm{d}x\mathrm{d}y$$
$$= (x - x_0) \log\left(R(x, y) + (y - y_0)\right) + (y - y_0) \log\left(R(x, y) + (x - x_0)\right)$$
$$\left. \left. -z_0 \arctan\left(\frac{(x - x_0)(y - y_0)}{z_0 R(x, y)}\right) + z_0 \arctan\left(\frac{(y - y_0)}{z_0}\right) - (y - y_0) \right|_{x=-1} \right|_{y=-1} . \tag{40}$$

Note that there is no issue with evaluating the arctangent when $z_0 = 0$, as the multiplication by z_0 yields zero. Also, we need to be careful using this antiderivative when evaluating cases where $z_0 = 0$ and $|x_0| = |y_0| = 1$. In that case, the integral simplifies to

$$\int_{-1}^{1} \int_{-1}^{1} \frac{1}{\sqrt{1 + x^2}} \, \mathrm{d}x\mathrm{d}y = 4 \sinh^{-1}(1). \tag{41}$$

Next, we consider the second part of integral equation (38), I_2, which we index with m and n

$$I_2 = \int_{-1}^{1} \int_{-1}^{1} \frac{(\vec{x} - \vec{x}_0)_m (\vec{x} - \vec{x}_0)_n}{R(x, y)^3} \, \mathrm{d}x\mathrm{d}y. \tag{42}$$

Note that the numerator in equation (42), written in index notation, refers to four different cases. There are two square-like terms

(a) $(x - x_0)(x - x_0)$ or $(y - y_0)(y - y_0)$ and (b) z_0^2,

and two mixed terms

(c) $(x - x_0)(y - y_0)$ and (d) $-(x - x_0)(z_0)$ or $-(y - y_0)(z_0)$.

Again, we treat $x_0 = y_0 = z_0 = 0$ separately. The first two diagonal terms (case (a)) are then

$$\int_{-1}^{1} \int_{-1}^{1} \frac{x^2}{(x^2 + y^2)^{3/2}} \, \mathrm{d}x\mathrm{d}y = 4 \arcsinh(1). \tag{43}$$

The third diagonal term is zero because here $z_0 = 0$, and every non-diagonal term is zero by symmetry.

26

Assuming that $x_0 y_0 z_0 \neq 0$, we consider cases (a)-(d) in turn. For case (a), we have

$$\int_{-1}^{1} \int_{-1}^{1} \frac{(x - x_0)^2}{R(x, y)^3} \, \mathrm{d}x \mathrm{d}y = (y - y_0) \left(\log \left(R(x, y) + x \right) - 1 \right)$$

$$+ z_0 \arctan \left(\frac{(y - y_0)}{z_0} \right) - z_0 \arctan \left(\frac{(x - x_0)(y - y_0)}{z_0 R(x, y)} \right) \Big|_{x=-1}^{1} \Big|_{y=-1}^{1} . \tag{44}$$

This case does not have evaluation issues since the argument of the logarithm can only be zero if $y = y_0$, which causes this entire term to be zero. Also, $R(x, y)$ can only be zero if $z_0 = 0$, which would then ensure that the third term would be zero. Note that the cases with numerator $(y - y_0)^2$ and $(x - x_0)^2$ are equivalent if we swap the x and y variables by choosing a different mapping.

Case (b) is simpler since the z_0 term is constant.

$$\int_{-1}^{1} \int_{-1}^{1} \frac{z_0^2}{R(x, y)^3} \, \mathrm{d}x \mathrm{d}y = z_0 \arctan \left(\frac{(x - x_0)(y - y_0)}{z_0 R(x, y)} \right) \Big|_{x=-1}^{1} \Big|_{y=-1}^{1} \tag{45}$$

Here, the only possibility to have an undefined value is when $z_0 = 0$, which simply gives a value of zero as the multiplying factor z_0 dominates the arctangent.

For case (c), we find

$$\int_{-1}^{1} \int_{-1}^{1} \frac{(x - x_0)(y - y_0)}{R(x, y)^3} \, \mathrm{d}x \mathrm{d}y = -R(x, y) |_{x=-1}^{1} \Big|_{y=-1}^{1} . \tag{46}$$

Finally, for case (d), we have

$$\int_{-1}^{1} \int_{-1}^{1} \frac{(x - x_0) z_0}{R(x, y)^3} \, \mathrm{d}x \mathrm{d}y = -z_0 \log \left(R(x, y) + (y - y_0) \right) |_{x=-1}^{1} \Big|_{y=-1}^{1} . \tag{47}$$

As before, this case also does not have any issue since $R(x, y) + (y - y_0)$ can only be zero if $z_0 = 0$, which causes the entire term to be zero.

A.2 Double-layer potential

We now consider the double-layer potential integrals of the form

$$\int_{S} \frac{(\vec{x} - \vec{x}_0)(\vec{x} - \vec{x}_0)}{R(x, y)^5} (\vec{x} - \vec{x}_0) \cdot n_k \, \mathrm{d}S(\vec{x}). \tag{48}$$

Since the inner product between the position and normal vectors always gives z_0 in the mapped coordinates, we focus on the integral,

$$\int_{S} \frac{(\vec{x} - \vec{x}_0)_m (\vec{x} - \vec{x}_0)_n}{R(x, y)^5} \, \mathrm{d}S(\vec{x}). \tag{49}$$

Note that we only need to compute this integral when $z_0 \neq 0$, as otherwise equation (48) is zero because of the inner product. This also implies that $R(x, y)$ may never be zero.

We now consider the following four cases:
(a) $m = n = 1$ or $m = n = 2$,
(b) $m = n = 3$,

27

(c) $m = 1$, $n = 2$ or $m = 2$, $n = 1$,

(d) $m = 1$ or 2 and $n = 3$, or $m = 3$ and $n = 1$ or 2 vice versa.

For case (a), we find

$$\int_{-1}^{1}\int_{-1}^{1}\frac{(x-x_0)^2}{R(x,y)^5}\,\mathrm{d}x\mathrm{d}y = \frac{1}{3}\left[\frac{1}{z_0}\arctan\left(\frac{(x-x_0)(y-y_0)}{z_0 R(x,y)}\right) - \frac{(x-x_0)(y-y_0)}{\left((x-x_0)^2+z_0^2\right)R(x,y)}\right]\Bigg|_{x=-1}^{1}\Bigg|_{y=-1}^{1}. \quad (50)$$

Since $z_0 \neq 0$ and $R(x,y) \neq 0$, there are no issues when evaluating this antiderivative.

For case (b),

$$\int_{-1}^{1}\int_{-1}^{1}\frac{z_0^2}{R(x,y)^5}\,\mathrm{d}x\mathrm{d}y = \frac{1}{3}\left[\frac{1}{z_0}\arctan\left(\frac{(x-x_0)(y-y_0)}{z_0 R(x,y)}\right)\right.$$
$$\left. + \frac{(x-x_0)(y-y_0)\left(R(x,y)^2+z_0^2\right)}{\left((x-x_0)^2+z_0^2\right)\left((y-y_0)^2+z_0^2\right)R(x,y)}\right]\Bigg|_{x=-1}^{1}\Bigg|_{y=-1}^{1}, \quad (51)$$

which again can always be evaluated directly when $z_0 \neq 0$.

Case (c) is relatively simple, as we can see,

$$\int_{-1}^{1}\int_{-1}^{1}\frac{(x-x_0)(y-y_0)}{R(x,y)^5}\,\mathrm{d}x\mathrm{d}y = \frac{1}{3R(x,y)}\Bigg|_{x=-1}^{1}\Bigg|_{y=-1}^{1}. \quad (52)$$

Finally, case (d) is

$$\int_{-1}^{1}\int_{-1}^{1}\frac{(x-x_0)z_0}{R(x,y)^5}\,\mathrm{d}x\mathrm{d}y = -\frac{(y-y_0)z_0}{3\left((x-x_0)^2+z_0^2\right)R(x,y)}\Bigg|_{x=-1}^{1}\Bigg|_{y=-1}^{1}. \quad (53)$$

Once again, this is simple to evaluate when $z_0 \neq 0$.

B Extensional Flow past a Sphere

In the case of a sphere of radius R_s, one may compute an exact solution for the flow satisfying $\vec{U}_{bg} = \bar{\bar{M}}\cdot\vec{x}$ at infinity and $\vec{U}_{bg} = 0$ on the surface of the sphere.

The Stokes flow around the sphere is then [53]

$$\vec{u} = \left(\bar{\bar{M}}\cdot\vec{x}\right)\left(1 - \frac{R_s^5}{r^5}\right) + \left((\bar{\bar{M}}:\vec{x}\vec{x})\vec{x}\right)\left(\frac{5}{2}\right)\left(\frac{R_s^5}{r^7} - \frac{R_s^3}{r^5}\right)$$

and the corresponding pressure is

$$P = -5\mu R_s^3\frac{\bar{\bar{M}}:\vec{x}\vec{x}}{r^5}$$

where $\vec{x}$ is the position vector and r the distance to the center of the sphere. The stress tensor is then

$$\bar{\bar{T}} = 5\mu R_s^3\frac{\bar{\bar{M}}:\vec{x}\vec{x}}{r^5} + 2\bar{\bar{M}}\left(1 - \frac{R_s^5}{r^5}\right)\cdot + (\vec{x}(\bar{\bar{M}}\cdot\vec{x}) + (\bar{\bar{M}}\cdot\vec{x})\vec{x})\left(\frac{10R_s^5}{r^7} - \frac{5R_s^3}{r^5}\right)$$
$$+ 5\left(\frac{R_s^5}{r^7} - \frac{R_s^3}{r^5}\right)(\bar{\bar{M}}:\vec{x}\vec{x})\bar{\bar{I}} + 5\left(\frac{5R_s^3}{r^7} - \frac{7R_s^5}{r^9}\right)(\bar{\bar{M}}:\vec{x}\vec{x})\vec{x}\vec{x}$$

On the surface of the sphere, where $r = R_s$, we consider the stress vector, $\vec{f} = \bar{\bar{T}} \cdot \hat{n}$, where $\hat{n} = \vec{x}/R_s$, and find

$$\vec{f} = \bar{\bar{T}} \cdot \hat{n}\Big|_{r=R_s} = \frac{5\mu}{R_s^2}\left(\frac{2\bar{\bar{M}} : \vec{x}\vec{x}}{R_s} - \frac{2\bar{\bar{M}} : \vec{x}\vec{x}}{R_s} + \bar{\bar{M}} \cdot \vec{x}R_s\right) = \frac{5\mu\bar{\bar{M}} \cdot \vec{x}}{R_s}$$

For an eigenvector $\hat{v}_i$ with eigenvalue λ_i, we thus find

$$S_i = \frac{1}{2}\int_S |\vec{f} \cdot \vec{v}_i|\, dS = 5\pi\mu R_s^2 \lambda_i.$$

References

[1] S. Honjo, T. Eglinton, C. Taylor, K. Ulmer, S. Sievert, A. Bracher, C. German, V. Edgcomb, R. Francois, M. Iglesias-Rodríguez, B. Van Mooy, D. Rapeta, Understanding the Role of the Biological Pump in the Global Carbon Cycle: An Imperative for Ocean Science, Oceanography 27 (3) (2014) 10–16.

[2] T. Kiørboe, Colonization of marine snow aggregates by invertebrate zooplankton: Abundance, scaling, and possible role, Limnology and Oceanography 45 (2) (2000) 479–484.

[3] T. Kiørboe, H.-P. Grossart, H. Ploug, K. Tang, Mechanisms and rates of bacterial colonization of sinking aggregates, Applied Environmental Microbiology 68 (8) (2002) 3996–4006.

[4] A. Alldredge, C. Gotschalk, In situ settling behavior of marine snow, Limnology and Oceanography 33 (3) (1988) 339–351.

[5] A. Burd, G. Jackson, Particle Aggregation, Annual Review of Marine Science 1 (1) (2009) 65–90.

[6] G. Jackson, A. Burd, Aggregation in the marine environment, Environmental Science and Technology 32 (19) (1998) 2805–2814.

[7] G. Jackson, Simulation of bacterial attraction and adhesion to falling particles in an aquatic environment, Limnology and Oceanography 34 (3) (1989) 514–530.

[8] G. Jackson, A model of the formation of marine algal flocs by physical coagulation processes, Deep-Sea Research 37 (1990) 1197–1211.

[9] S. MacIntyre, A. Alldredge, C. Gotschalk, Accumulation of marines now at density discontinuities in the water column, Limnology and Oceanography 40 (3) (1995) 449–468.

[10] A. Alldredge, T. Cowles, S. MacIntyre, J. Rines, P. Donaghay, C. Greenlaw, D. Holliday, M. Dekshenieks, J. Sullivan, J. Zaneveld, Occurrence and mechanisms of formation of a dramatic thin layer of marine snow in a shallow Pacific fjord, Marine Ecology Progress Series 233 (2002) 1–12.

[11] J. C. Prairie, K. Ziervogel, C. Arnosti, R. Camassa, C. Falcon, S. Khatri, R. McLaughlin, B. White, S. Yu, Delayed settling of marine snow at sharp density transitions driven by fluid entrainment and diffusion-limited retention, Marine Ecology Progress Series 487 (2013) 185–200.

[12] R. Camassa, S. Khatri, R. M. McLaughlin, J. C. Prairie, B. L. White, S. Yu, Retention and entrainment effects: Experiments and theory for porous spheres settling in sharply stratified fluids, Physics of Fluids 25 (8) (2013) 081701.

[13] M. Panah, F. Blanchette, S. Khatri, Simulations of a porous particle settling in a density-stratified ambient fluid, Physical Review Fluids 2 (11) (2017) 114303.

[14] H. Rosenstock, C. Marquardt, Cluster formation in two-dimensional random walks: Application to photolysis of silver halides, Physical Review B 22 (12) (1980) 5797–5809.

[15] T. A. Witten, L. M. Sander, Diffusion-limited aggregation, a kinetic critical phenomenon, Physical Review Letters 47 (19) (1981) 1400–1403.

[16] T. A. Witten, M. E. Cates, Tenuous structures from disorderly growth processes, Science 232 (4758) (1986) 1607–1612.

[17] M. Kolb, Anisotropic diffusion limited aggregation: From self-similarity to self-affinity, EuroPhysics Letters 4 (1) (1987) 85–90.

[18] P. Wiltzius, Hydrodynamic behavior of fractal aggregates, Physical Review Letters 58 (7) (1987) 710–713.

[19] M. Takayasu, F. Galembeck, Determination of the equivalent radii and fractal dimension of polystyrene latex aggregates from sedimentation coefficients, Journal of Colloid and Interface Science 202 (1) (1998) 84–88.

[20] C. Johnson, X. Li, B. Logan, Settling velocities of fractal aggregates, Environmental Science and Technology 30 (6) (1996) 1911–1918.

[21] P. Tang, J. Greenwood, J. A. Raper, A model to describe the settling behavior of fractal aggregates, Journal of Colloid and Interface Science 247 (1) (2002) 210–219.

[22] Z. Chen, J. Deutch, P. Meakin, Translational friction coefficient of diffusion limited aggregates, The Journal of Chemical Physics 80 (6) (1984) 2982–2983.

[23] J. Brady, G. Bossis, Stokesian Dynamics, Annual Review of Fluid Mechanics 20 (1) (1988) 111–157.

[24] S. Rogak, R. Flagan, Stokes drag on self-similar clusters of spheres, Journal of Colloid and Interface Science 134 (1) (1990) 206–218.

[25] G. Bossis, A. Meunier, J. Brady, Hydrodynamic stress on fractal aggregates of spheres, Journal of Chemical Physics 94 (7) (1991) 5064–5070.

[26] C. Binder, M. Hartig, W. Peukert, Structural dependent drag force and orientation prediction for small fractal aggregates, Journal of Colloid and Interface Science 331 (1) (2009) 243–250.

[27] J. Zhang, Q. Zhang, Direct Simulation of Drag Force on Fractal Flocs during Settling, Journal of Coastal Research, 73 (sp1) (2015) 753–757.

[28] A. Gastaldi, M. Vanni, The distribution of stresses in rigid fractal-like aggregates in a uniform flow field, Journal of Colloid and Interface Science 357 (1) (2011) 18–30.

[29] M. Vanni, Accurate modelling of flow induced stresses in rigid colloidal aggregates, Computer Physics Communications 192 (2015) 70–90.

[30] C. Pozrikidis, Boundary Integral and Singularity Methods for Linearized Viscous Flow, Cambridge University Press, Cambridge, England, 1992.

[31] C. Pozrikidis, Interfacial dynamics for Stokes Flow, Journal of Computational Physics 169 (2001) 250–301.

[32] A. Z. Zinchenko, R. H. Davis, A boundary-integral study of a drop squeezing through interparticle constrictions, Journal of Fluid Mechanics 564 (10) (2006) 227–266.

[33] Y. Bao, A. Donev, B. E. Griffith, D. M. McQueen, C. S. Peskin, An immersed boundary method with divergence-free velocity interpolation and force spreading, Journal of Computational Physics 347 (2017) 183–206.

[34] Y. Bao, M. Rachh, E. E. Keaveny, L. Greengard, A. Donev, A fluctuating boundary integral method for Brownian suspensions, Journal of Computational Physics 374 (2018) 1094–1119.

[35] R. Cortez, The Method of Regularized Stokeslets, SIAM Journal of Scientific Computing 23 (4) (2001) 1204–1225.

[36] K. Atkinson, The Numerical Solution of Integral Equations of the Second Kind, Cambridge University Press, Cambridge, England, 1997.

[37] L. Delves, J. Mohamed, Computational Methods for Integral Equations, Cambridge University Press, Cambridge, England, 1985.

[38] C. Chan, A. Beris, S. Advani, Second-order boundary element method calculations of hydrodynamic interactions between particles in close proximity, International Journal for Numerical Methods in Fluids 14 (9) (1992) 1063–1086.

[39] D. Smith, A nearest-neighbour discretisation of the regularized stokeslet boundary integral equation, Journal of Computational Physics 358 (2018) 88–102.

[40] H. Power, G. Miranda, Second kind integral equation formulation of Stokes' flows past a particle of arbitrary shape, SIAM Journal of Applied Mathematics 47 (4) (1987) 689–698.

[41] M. Ingber, A. Mammoli, A comparison of integral formulations for the analysis of low Reynolds number flows, Engineering Analysis with Boundary Elements 23 (4) (1999) 307–315.

[42] L. Gmachowski, Calculation of the fractal dimension of aggregates, Colloids and Surfaces A: Physicochemical and Engineering Aspects 211 (2) (2002) 197–203.

[43] M. Eggersdorfer, D. Kadau, H. Herrmann, S. Pratsinis, Multiparticle Sintering Dynamics: From Fractal-Like Aggregates to Compact Structures, Langmuir 27 (10) (2011) 6358–6367.

[44] B. Logan, D. Wilkinson, Fractal geometry of marine snow and other biological aggregates, Limnology and Oceanography 35 (1) (1990) 130–136.

[45] B. Kaye, A Random Walk Through Fractal Dimensions, 2nd Edition, Wiley-VCH, Weinheim, Germany, 1994.

[46] I. Stakgold, Boundary Value Problems of Mathematical Physics: Volume 2, Classics in Applied Mathematics, SIAM, 2000.

[47] G. K. Youngren, A. Acrivos, Stokes flow past a particle of arbitrary shape: a numerical method of solution, Journal of Fluid Mechanics 69 (2) (1975) 377–403.

[48] S. Gurel, S. G. Ward, R. L. Whitmore, Studies of the viscosity and sedimentation of suspensions: Part 3. - The sedimentation of isometric and compact particles, British Journal of Applied Physics 6 (3) (1955) 83–87.

[49] D. Johnson, D. Leith, P. Reist, Drag on non-spherical, orthotropic aerosol particles, Journal of Aerosol Science 18 (1) (1987) 87–97.

[50] J. McNown, J. Malaika, Effects of particle shape on settling velocity at low Reynolds numbers, Eos, Transactions American Geophysical Union 31 (1) (1950) 74–82.

[51] L. Delves, Numerical solution of integral equations, Clarendon Press,, Oxford, England, 1974.

[52] S. Karrila, S. Kim, Integral equations of the second kind for Stokes flow: Direct solution for physical variables and removal of inherent accuracy limitations, Chemical Engineering Communications 82 (1) (1989) 123–161.

[53] E. Guazzelli, J. Morris, , S. Pic, A Physical Introduction to Suspension Dynamics, Cambridge University Press, Cambridge, England, 2012.